

DRG-Net: Interactive Joint Learning of Multi-lesion Segmentation and Classification for Diabetic Retinopathy Grading

Hasan Md Tusfiqu^{1,*}, Duy M. H. Nguyen^{1,2,*}, Mai T. N. Truong³, Triet A. Nguyen⁴, Binh T. Nguyen⁵, Michael Barz¹, Hans-Jürgen Profitlich¹, Ngoc T. T. Than⁶, Ngan Le⁷, Pengtao Xie⁸, Daniel Sonntag^{1,9}

Abstract—Diabetic Retinopathy (DR) is a leading cause of vision loss in the world, and early DR detection is necessary to prevent vision loss and support an appropriate treatment. In this work, we leverage interactive machine learning and introduce a joint learning framework, termed DRG-Net, to effectively learn both disease grading and multi-lesion segmentation. Our DRG-Net consists of two modules: (i) DRG-AI-System to classify DR Grading, localize lesion areas and provide visual explanation and (ii) DRG-Expert-Interaction to receive feedback from user-expert and improve the DRG-AI-System. To deal with sparse data, we utilize transfer learning mechanisms to extract invariant feature representations by using Wasserstein distance and adversarial learning-based entropy minimization. Besides, we propose a novel attention strategy at both low- and high-level features to automatically select the most significant lesion information and provide explainable properties. In terms of human interaction, we further develop DRG-Net as a tool that enables expert users to correct the system’s predictions, which may then be used to update the system as a whole. Moreover, thanks to the attention mechanism and loss functions constraint between lesion features and classification features, our approach can be robust given a certain level of noise in the feedback of users. We have benchmarked DRG-Net on the two largest DR datasets, i.e., IDRID and FGADR, and compared it to various state-of-the-art deep learning networks. In addition to outperforming other SOTA approaches, DRG-Net is effectively updated using user feedback, even in a weakly-supervised manner.

I. INTRODUCTION

Diabetes is a chronic health condition that is estimated to affect about one in every ten people worldwide Saeedi et al. (2019). According to Yang et al. (2021), 40% to 45% of people with diabetes may develop *Diabetic Retinopathy (DR)* during their lifetime. DR is a kind of ocular disease that damages the retina’s blood vessels, and it is one of the leading causes of irreversible blindness. Although the symptoms are diagnosed only in the later stage, people suffering from this disease start to lose vision from an early stage. To assess the

complexity of DR, *International Clinical Diabetic Retinopathy Disease Severity Scale* Gulshan et al. (2016) has used five grades (0-4), including *no DR*, *mild*, *moderate*, *severe*, and *proliferative* as shown in Figure 1. In practice, accurate DR grading is a time-consuming task and there is a huge shortage of qualified ophthalmologists. Therefore, an automated system can significantly aid the diagnosis process.

While the existing methods Gulshan et al. (2016); Antal and Hajdu (2012); Wang et al. (2017) can assist ophthalmologists in validating and interpreting the automated prediction, they introduce three main issues: (i) They are designed as black-box models and unable to utilize lesion features to improve the models. (ii) Lesion segmentation performance is limited because of irregularities in shape, noisy, ill-defined boundaries, intra-class lesion diversities and less labeled data, (iii) Though disease classification and lesion discovery are strongly correlated, they are mostly studied as independent tasks.

Joint learning has recently shown promising progress in medical imaging e.g., breast cancer Mehta et al. (2018), skin lesion Al-Masni et al. (2020), COVID-19 detection Nguyen et al. (2021b); Wu et al. (2021), and retinal blood vessel Li et al. (2020). However, the performance of joint learning-based medical imaging is generally limited due to domain-shift and scarcity of labeled data. To address the aforementioned limitations, we propose a joint learning-based multi-lesion segmentation and classification for DR Grading, termed DRG-Net. Our DRG-Net includes a novel *Domain Invariant Lesion Feature Generator* and *Attention-Based Disease Grading Classifier*. While the former aims to identify and distinguish important lesion regions of different semantics, the later one aims to incorporate the predicted lesion information in the learning process of the disease classification network. Furthermore, our framework is designed as a collaborative learning system between user and machine learning (ML) model, i.e., (i) ML model provides both lesion prediction with its corresponding relevant clinical evidence; (ii) the system allows users to inspect the predicted results and be able to enhance accuracy given new samples which are roughly annotated by users, e.g., drawing a bounding box around lesion regions rather than a precise segmentation boundary.

Our contributions are summarized as followed:

- We construct a novel lesion segmentation model by formulating a domain invariant learning scheme combining a new transfer learning scheme and domain adaption concepts.

*Equal contribution

¹German Research Center for Artificial Intelligence (DFKI)

²Machine Learning and Simulation Lab, University of Stuttgart, Germany

³Department of Multimedia Engineering, Dongguk University, South Korea

⁴Department of Mathematics, University of Architecture Ho Chi Minh City

⁵AISIA Lab, University of Science - VNUHCM, Vietnam

⁶Byers Eye Institute, Stanford University, USA

⁷Department of Computer Science and Computer Engineering, University of Arkansas, USA

⁸Department of Electrical and Computer Engineering, University of California San Diego, USA,

⁹Applied Artificial Intelligence, Oldenburg University, Germany

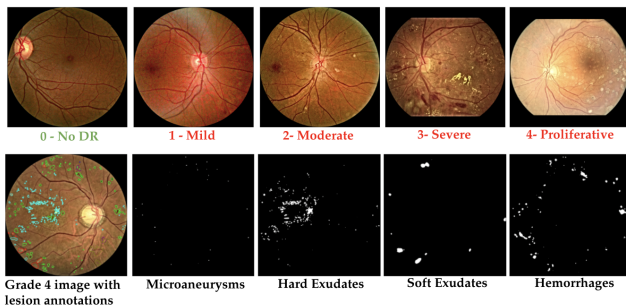


Fig. 1: Illustration of diabetic retinopathy retinal images. Top row - examples of different stages of DR disease. Bottom row - a retinal image with lesion information annotated by domain expert (left most image). The remaining 4 images are lesion mask predicted by the Dense U-Net Segmentation model Zhou et al. (2020); Li et al. (2018b).

- We address both the challenges of scarcity of labeled data and domain shift.
- We train our segmentation model with adversarial learning Goodfellow et al. (2014) to enhance its robustness and accuracy.
- Our framework is explainable and provides diverse information to the end-users with interpretation to support its decision.
- Our framework allows user to provide feedback on the output and if required, re-annotate the predicted lesion features, which can be used to fine-tune the model further.
- Our learning method can be robust to a certain threshold, and pixel-wise correction is not required.
- We conduct comprehensive experiments and compare with the recent state-of-the-art methods to illustrate the effectiveness of our proposed DRG-Net.

The rest of the paper is organized as follows: In section II, we review some of the related works and some preliminaries for our method. Next, we detail our proposed DRG-Net in section IV. Our DRG-Net is evaluated and compared with other SOTA existing work in section VI. Finally, we discuss the proposed method and future

II. RELATED WORK

A. DR Grading Analysis

DR Grading analysis aims to classify fundus images into different DR severity classes and extract the relevant lesion regions. Most of early works focus on classification task only, i.e. classifying DR into multiple classes of grading Gulshan et al. (2016); Sankar et al. (2016); Alban and Gilligan (2016). However, such existing approaches treat the problem of classification task as a *black box* and did not consider the fine-grained DR-related lesion information in the learning process Nguyen et al. (2021a); Zhou et al. (2020). Some recent approaches attempt to integrate lesion information to improve the grading classification. For instance, Yang et al. (2017) propose two-stages Convolutional Neural Networks (CNNs), which contains two CNNs: the former plays the role of local network and aims to learn a weighted attention lesion

map; the later plays the role of global network and exploits image features in holistic level for DR grading by utilizing the former's outcomes. Lin et al. (2018) propose a similar framework to automatically detect missing lesion features and integrate with global image features using a classification network for grading prediction.

However, the aforementioned approaches are designed in a cascade framework i.e., extract lesion information first and then classify DR Grading. With such network design, both tasks are optimized independently while they have a strongly coherency. To address such limitation, Zhou et al. (2019) propose a collaborative learning pipeline to jointly learn both lesion segmentation and DR Grading classification by semi-supervised learning with an attention mechanism. Lately, Yang et al. (2021) also introduce an attention-based learning scheme, which collaboratively learns to predict lesion maps patches and DR grading. Leveraging multi-head attention mechanism, Sun et al. (2021) combine self-attention and cross-attention mechanisms to direct the overall attention of a network to consider lesion region diversity and their importance separately in the final DR grading prediction. While obtaining promising performance, these methods suffer from *domain shift problem* i.e. difference in data distribution between source (used to train the model) and target (encountered during inference). Furthermore, none of the exiting approaches can explain how lesion maps influences the final DR grading prediction while lesion regions do not share the same contribution to DR grade. In this paper, we propose an explainable interactive joint learning framework, which does not only results lesion localization and its corresponding DR Grading score but also provides an informative explanation of the outcomes.

B. Visual explanations of CNNs.

Explaining the CNNs prediction is crucial for the system acceptance in critical applications such as DR Grading. In general, generating saliency maps that highlight the image regions contributing to the final CNNs prediction is one of the most common techniques. There have been a large number of research proposed to visualize a CNNs predictions by highlighting important regions that are believed to be intuitive to end-users.

For instance in image classification, visual explanation is considered to be good if it is able to be localize the category in the image (i.e. class-discriminative). Class Activation Mapping (CAM) Zhou et al. (2016) is considered as one of the most common technique for identifying informative areas by a CNNs-based classification. In short, CAM utilizes the last convolutional layer and combine weighted activation maps to produce explainable heatmaps. As a result, it is highly class-discriminative, however, the output heatmaps is blurry (low-resolution). As an improvement of CAM, Selvaraju et al. (2017) propose Grad-CAM, which does not require any specific network architecture. However, gradients can be noisy and may get vanished in activation function like sigmoid, ReLU. To address this issue, Wang et al. (2020) proposed Score-CAM, which gets rid of the dependence on gradients by obtaining the weight of each activation map. In Score-CAM, the final result is obtained by a linear combination

of weights and activation maps. Furthermore, to address the problem of low-resolution heatmaps, Jalwana et al. (2021) propose CAMERAS to produce high-resolution heatmaps with multi-scale accumulation and fusion of the activation maps and backpropagated gradients to compute precise saliency maps. CAM-based explainable mechanisms have been recently utilized by many research in medical imaging. For example, Nguyen et al. (2021b) proposed a CAM-based explainable COVID-19 detection method using CT images, Wu et al. (2021) adopt the Grad-CAM technique to perform the joint task of classification and segmentation for COVID-19 detection. In this work, we propose a constraint between heatmap regions computed by GradCam in Grading Network with multi-lesion regions extracted by Lesion generators. This step aim to generate lesion prior-guided DR grading predictions. Additionally, the proposed distilling strategy using attention mechanism enables automatically selecting major lesion parts used in specific disease grading tasks and making the model to be robust. This sets us apart with other works Nguyen et al. (2021b); Wu et al. (2021). In the experiments, we demonstrate that this tactic improves prediction performance and provide helpful explanations to the experts (Figures 2 and 15).

C. Transfer learning and Domain Adaptation

Domain adaptation can be regarded as a special case kind of transfer learning, thus, we first review the definitions of each to provide the differences. In the standard transfer learning setting, there are two main concepts: domain and task. While domain means the feature space of a particular dataset and the marginal probability distribution of features, task means the label space of a dataset and an specific objective function. In general, transfer learning aims to transfer the knowledge learned from a task \mathcal{T}_a on domain \mathcal{A} (i.e. source) to another task \mathcal{T}_B on domain \mathcal{B} (i.e target). Domain adaptation, as a special case of transfer learning, it assumes that both source and target share the same domain feature spaces and tasks and whereas only marginal distributions between the source and target domains are different. In medical image analysis (MIA), domain adaptation and transfer learning have been promisingly used for dealing with limited labeled data issue.

Transfer Learning in MIA: Rather than training a network with limited training data from a target task, the network is first trained for a task with potentially larger source datasets, creating a more robust model. This pre-trained network is then down-streamed on target task. However, a large-scale analysis by Cheplygina (2019); He et al. (2020) suggests that transfer learning might be not better than random initialization for most medical tasks. Medical images are significantly different from the natural image (e.g. ImageNet dataset); therefore, features learned from the external data maybe not effective helpful for the target medical domain task. Furthermore, medical data often face to the problem of imbalanced data at both instance level and pixel level Le et al. (2021). To address those limitations, Nguyen et al. (2022b) propose a novel transfer learning, termed *Task Agnostic Transfer Learning (TATL)*, motivated by dermatologists' behavior in the skincare context. TATL is learnt by a two-stage learning step i.e.,

first, an attribute-agnostic network is trained, which detects all the lesion regions irrespective of their labels; then, the knowledge from this network is transferred to a set of attribute-specific classifiers to label each particular region. However, the performance of DNN trained on a particular source domain and transferred to a different target domain (e.g., different vendor, acquisition parameters), can drop unexpectedly due to domain shift. Yan et al. (2019).

Domain Adaptation in MIA: In this settings, the networks are trained with domain adaptation constraints to address the domain-shift problem. Tzeng et al. (2014) proposed a Deep Domain Confusion (DDC) method to reduce the divergence between two distributions by minimizing the maximum mean discrepancy (MMD) loss (Gretton et al., 2012). MMD is a nonparametric metric and can be used to compute distances between distributions as distances between mean embeddings of features. In their method, a network is trained with data from multiple distributions using a loss function that consists of both task-specific loss and MMD loss. Some studies apply adversarial optimization to remove the domain discrepancy by incorporating generative adversarial networks (GANs). GANs consists of two networks, i.e., a generator to generate a new data from a distribution and a discriminator to evaluate the new data Goodfellow et al. (2014). The two networks trained using game theory theorem, i.e. minimax. Tzeng et al. (2017) combined standard adversarial loss with the task-specific classification loss to minimize domain distances. At first, a discriminative model (e.g. CNNs) is trained using labeled data from the source domain. Then, a target encoder is learned using GANs adaptation, where discriminator aims to distinguish between encoded source and target examples. Shen et al. (2018) describe Wasserstein distance guided representation learning (WDGRL) method to reduce the domain discrepancy by minimizing Wasserstein distance for each feature block of the encoder CNN.

In this work, we are the first take into accounts transfer learning and domain adaptation problems in the context of DR-Grading and Segmentation. These issues in fact are typically encountered when deploying an AI-assisted system in medicine applications, thus a robust framework under circumstances is critical. To this end, we properly designed support deep networks (PD-Net, AD-Net and W-Net) that jointly learn with lesion generator S-Nets. These support network operate based on the cutting-edge domain adaptation and adversarial leaning techniques which have been shown impressing results on various applications such as object recognition, self-driving car, etc. In experiments, we demonstrate that all of these components contribute to improve performance and robustness.

D. Interactive Machine Learning

Interactive Machine Learning (IML), which focuses on interaction between users and learning systems Amershi et al. (2014), with people interactively supplying information in a more focused, frequent, and incremental way compared to traditional ML. Typically, IML is an active ML technique in which models are designed and implemented with human-in-the-loop manner. While ML algorithms usually requires

a large-scale data to yield accurate result; however, such requirement is limited in some domains like clinical trials, medical analysis. A comprehensive review of IML medical analysis is extensively studied in Maadi et al. (2021). To build such a computer-based interactive system, the initial challenge is how to represent the semantics in a machine-readable form using medical ontologies Sonntag et al. (2010) so that the information is easily exchangeable between human experts and machines. RadSpeech’s *Mobile Dialogue System for Radiologist* Sonntag et al. (2012) provides a multi-modal interaction system for radiology image annotations. It is a user-friendly semantic search interface where users can annotate medical image regions with a specific medical, structured diagnosis using speech and pointing gestures. Prange et al. (2017) presents a medical decision support system inside virtual reality (VR). In this system, a doctor can visualize patients’ records and clinical images, as well as therapy predictions which are computed in real-time using a pre-trained deep learning model. The aforementioned studies provide the techniques to capture user feedback (annotations on inputs) for an intelligent learning system. However, they did not consider the inclusion process of these feedbacks in an IML loop. Sonntag et al. (2020) describes the functionality and interface of an interactive decision support system for differential diagnosis of malignant skin lesions, where the user can re-annotate an input that is used to fine-tune the prediction model based on the explanation. Recently, Dai et al. (2021) presents a real-time deep learning based interactive system for diabetic retinopathy where the architecture consists of three sub-networks to perform different tasks one by one. However, the coherent relation between lesion discovery and disease classification was mostly ignored, making it hard to conclude that lesion-feature information predicted by the segmentation part has any influence on the classification result.

In this paper, we introduce the first time a human interactive framework for the DR-Grading and Segmentation tasks. The expert user benefit from our AI-assist system with the following advantageous. First, we provide an explainable predictions by correlation between heatmap of the classification network with medical lesion regions. This helps the doctor inspect predictions generated by system by bridging with their prior knowledge. Second, due to transfer learning and domain adaptation, we permit a fast deployment our system on a new domain (new hospital, new data, etc.) while not demanding large annotations to pre-train the system (only classification annotation is required, don’t need segmentation in beginning), leading to saving labour costs. Finally, the model is designed to learn from user’s feedback in weak and noise annotation forms (bounding boxes rather than precise segmentation masks, noise in new data can be damped through constraints among classification, segmentation, and attention loss functions).

III. DRG-NET: OVERVIEW AND PROBLEM SETUP

A. Overview

Our DRG-Net consists of two modules: (i) *DRG-AI-System* to classify DR Grading, localize lesion areas and provide

visual explanation and (ii) *DRG-Expert-Interaction* to receive feedback from user-expert and improve the DRG-AI-System. The overall framework of our proposed DRG-Net is depicted in Fig. 2. Given a retina image input, our first module DRG-AI-System will simultaneously returns three outputs: (a) DR grade severity on a scale of 0 to 4 by *Attention-based Classifier*, comprising Att-Net and G-Net, (b) lesion areas by *Feature generator*, comprising S-Nets and support systems (PD-Net, AD-Net, W-Net), (c) and a correlation among visual explanation, lesion regions and grading prediction. To address real-world challenges of DRG analysis including scarcity labeled data, small lesion localization, and domain shift, we propose to design DRG-AI-System in an unsupervised domain adaptation (UDA) manner, where the system was trained on source data with annotation and test on target data without label. In the second module of DRG-Expert-Interaction, the expert can provide feedback on the grading and lesion information, which is then utilized to fine-tune the DRG-AI-System network.

B. Problem Setup

In DRG-AI-System, we consider two correlated tasks at both image-level and pixel-level. The former task aims to classify DR Grading (i.e., associate an input image with a DR Grading class), whereas the later one aims to localize lesion areas (i.e., partition an input image into various lesion areas).

Let $\mathbf{x}_s \in \mathcal{X}_s$, $\hat{\mathbf{t}}_s \in \mathcal{T}_s$, and $\hat{\mathbf{y}}_s \in \mathcal{Y}_s$ be an input image and its corresponding image-level and pixel-level label in the source domain drawn from the source distribution p_s . Similarly, we denote $\mathbf{x}_t \in \mathcal{X}_t$, $\hat{\mathbf{t}}_t \in \mathcal{T}_t$ and $\hat{\mathbf{y}}_t \in \mathcal{Y}_t$ be the input image and its corresponding image-level and pixel-level label in the target domain drawn from the target distribution p_t . As for image-level label, there are C classes of No DR (0), Mild (1), Moderate (2), Severe (3), Proliferative (4). As for pixel-level label, there are L classes of Microaneurysms (MA), Hard Exudates (HE), Soft Exudates (SE), Hemorrhages (EX).

In our domain adaptation setting, the ground-truth pixel-level label $\hat{\mathbf{y}}_t$ of image \mathbf{x}_t is not available.

The DRG-AI-System is trained on source data and tested on target data. Given a target retinal image $\mathbf{x}_t \in \mathcal{X}_t$, the output from DRG-AI-System is a tuple of grading level, localizing lesion areas and explainable visual representation.

The following Table I summarizes and briefly describes important symbols that are used throughout this manuscript:

Each module will be detailed in the following sections.

IV. DRG-NET: DRG-AI-SYSTEM

Our proposed UDA DRG-AI-System consists of three main components: The first component, Feature Generator, plays the role of multi-lesion segmentation and is termed *S-Net*. The second component plays the role of UDA including Patch Discriminator *PD-Net*, Wasserstein Discriminator *W-Net* and Adversarial Domain Discriminator *AD-Net*. The second component aims to support the first component in dealing with scarcity labeled data, small objects and domain shift. The third component, Attention-based Classifier, is designed as a combination of an Attention Network *Att-Net* and a Grading Network *G-Net*. The overall DRG-AI-System is given in Fig. 5.

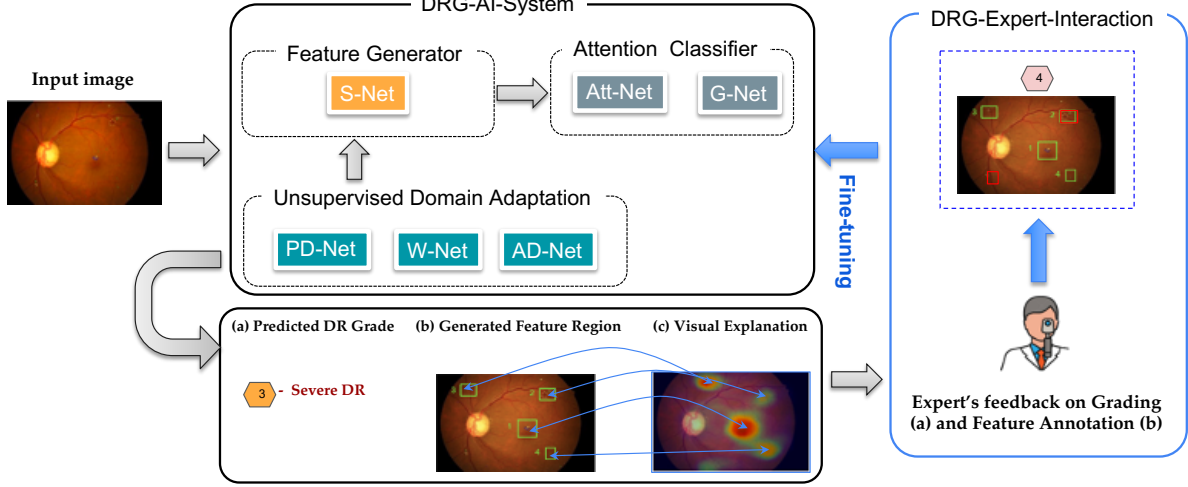


Fig. 2: A high-level overview of our proposed DRG-Net system that contains two main module of DRG-AI-System and DRG-Expert-Interaction. DRG-AI-System: Given a retinal image, our deep learning models will simultaneously generate three outcomes prediction (DR grade, lesion region, visual explanation). DRG-Expert-Interaction: By using an Intelligent User Interface (IUI), ophthalmologists can observe the system’s predictions and provide feedback to fine-tune the model.

TABLE I: Summation of symbols and their brief description.

Variables	Description	Network	Description
L	Number of classes of lesions	S-Net = $\{S^e, S^d\}$	Segmentation network, encoder S^e and decoder S^d
\mathcal{X}_s	source domain	$S_l = \{S_l^e, S_l^d\}$	Binary segmentation network for a lesion l
\mathcal{X}_t	target domain	PD-Net	Patch Discriminator
$\mathbf{x}_s \in \mathcal{X}_s$	an image in source domain	W-Net	Wasserstein Discriminator
$\mathbf{x}_t \in \mathcal{X}_t$	an image in target domain	AD-Net	Adversarial Domain Discriminator
\mathbf{x}	an image from any domain	Att-Net	Attention Network
$\hat{\mathbf{t}}_s, \hat{\mathbf{t}}_t$	GT image-level label of source/target image	G-Net	Grading Network
$\hat{\mathbf{y}}_s, \hat{\mathbf{y}}_t$	GT pixel-level label of source/target image		
$\hat{\mathbf{y}}$	predicted pixel-level label		
$\mathbf{h}_s, \mathbf{h}_t$	encoder feature map of a source/target image		
\mathbf{g}^i	Conv. block		
\mathbf{o}^i	output of each Conv. block \mathbf{g}^i		
h, w	height and width of an image		
C	number of grading labels		

A. Feature Generator: multi-lesion segmentation S-Net

S-Net aims to partition an input retinal image into L binary segmentation masks, each represents a lesion mask. In this paper, our proposed S-Net is based on an encoder-decoder Unet-like architecture Ronneberger et al. (2015) consisting of encoder S^e and decoder S^d .

Furthermore, we focus on real-world applications where S-Net is trained on source domain \mathcal{X}_s and tested on target domain \mathcal{X}_t . Under this setup, annotation is only available during training including image-level annotation $\hat{\mathbf{t}}_s \in \mathcal{T}_s$, and pixel-level annotation $\hat{\mathbf{y}}_s \in \mathcal{Y}_s$. Due to scarcity of training data, small lesion area and domain shift, standard Unet-based networks are limited when working on retinal images. In this work, we propose to utilize Task Agnostic Transfer Learning (TATL) framework Nguyen et al. (2022b) to propose a novel UDA approach to alleviate the aforementioned challenges. Our proposed UDA consists of three sub-networks, i.e. Patch Discriminator PD-Net, Wasserstein Discriminator W-Net and Adversarial Domain Discriminator AD-Net, which will be detailed in Section IV-B whereas we only focus describing S-Net in this section.

In the TATL settings, S-Net is first pre-trained at the pretext task on a multi-lesion region first. Then, it is then fine-tuned on the downstream task for segmenting an individual lesion region. Each particular lesion l is segmented by a network S_l , all $S_l, l \in [1, L]$ shares a similar network architecture as S-Net. For a given image $\mathbf{x}_s \in \mathcal{X}_s$, for each network S_l , we obtain a binary segmentation mask $S_l(\mathbf{x}_s)$, ($l \in L$), where $L = \{\text{MA, HE, SE, EX}\}$. The segmentation network is trained by weighted binary cross-entropy loss as follows:

$$\mathcal{L}_{seg} = \min \frac{1}{|\mathcal{X}_s|} \sum_{(\mathbf{x}_s, \hat{\mathbf{y}}_s) \in \mathcal{X}_s} \sum_{l \in L} \mathcal{L}_{wbce}(S^l(\mathbf{x}_s), \hat{\mathbf{y}}_{s_l}) \quad (1)$$

where $\hat{\mathbf{y}}_{s_l}$ is pixel-level annotation of lesion l . \mathcal{L}_{wbce} is the weighted binary cross-entropy loss

$$\mathcal{L}_{wbce}(\hat{\mathbf{y}}, \mathbf{y}) = -(\beta \cdot \hat{\mathbf{y}} \log(\mathbf{y}) + (1 - \hat{\mathbf{y}}) \log(1 - \mathbf{y})), \quad (2)$$

where $\hat{\mathbf{y}}$ is the ground-truth binary lesion mask and \mathbf{y} is the model prediction, β is the class balancing weight. The loss \mathcal{L}_{wbce} in general can be replaced with other segmentation losses Jadon (2020).

So far, we have trained the segmentation model S_l in the source domain \mathcal{X}_s using eq.1 where annotation is available. However, it is unfit to target domain where we do not have annotation. We propose to constrain the embedding space of the source and target domains are close to each other by minimizing Wasserstein distance Arjovsky et al. (2017); Liu et al. (2019) via *W-Net*. Furthermore, to improve semantic segmentation accuracy on tiny objects, we follow prior studies (Hung et al., 2018) and incorporate a discriminate network for each lesion segmentation model S_l . We propose Patch Discriminator *PD-Net*. Furthermore, to exploit the structural consistency between the source and target domain, we proposed *AD-Net* to directly minimize an uncertainty prediction in the target domain. Details of *PD-Net*, *W-Net* and *AD-Net* are in Section IV-B

B. Unsupervised Domain Adaptation

1) *Patch Discriminator PD-Net*: To improve semantic segmentation accuracy on tiny objects, we follow prior studies (Hung et al., 2018) and incorporate a discriminate network for each lesion segmentation model S_l . We propose Patch Discriminator *PD-Net*, a conditional GAN Mirza and Osindero (2014), which aims to distinguish *real* samples from the generated ones. The architecture of *PD-Net* is similar to Xiao et al. (2019), which is formed based on the ideas of PatchGAN Isola et al. (2017) as illustrated in Fig. 3 .

In particular, an input image is split into 16×16 smaller patches, and each of these patches is applied with the cross-entropy loss to decide whether that patch is fake or real. The input for the *PD-Net* is the concatenation of the original image patch with its corresponding lesion map predicted from S_l and actual ground truths. Thus, the discriminator *PD-Net* learns the joint distribution of both images and the lesion map, conditioned on the input data. In other words, the *PD-Net* will force the output of S_l to look 'real' as the ground-truth data as much as possible given the input image $\mathbf{x}_s \in \mathcal{X}_s$. The objective loss function for this formulation can be defined as:

$$\mathcal{L}_{\text{patch}} = \min_{\theta_{S_l}} \max_{\theta_{\text{pd}}} \frac{1}{|\mathcal{X}_s|} \sum_{(\mathbf{x}, \hat{\mathbf{y}}_l) \in \mathcal{X}_s} [\log(\text{PD}(\mathbf{x} \oplus \hat{\mathbf{y}}_l))] \quad (3)$$

$$+ \log(1 - (\text{PD}(\mathbf{x} \oplus \mathbf{y}_l))) \quad (4)$$

where θ_{S_l} and θ_{pd} are parameters of binary segmentation network S_l and *PD-Net*. \oplus is the concatenation operator. z_l is output of binary segmentation network S_l i.e., $z_l = S_l(\mathbf{x})$ and $\hat{\mathbf{y}}_l$ is groundtruth corresponding to lesion l . Combining this adversarial objective with Eq. (1), we derive an optimization problem for the segmentation model S_l using the source domain \mathcal{X}_s as:

$$\mathcal{L}_{\text{source}} = \mathcal{L}_{\text{seg}} + \lambda_p \mathcal{L}_{\text{patch}}. \quad (5)$$

where λ_p is a parameter controls the contribution of $\mathcal{L}_{\text{patch}}$.

2) *Wasserstein Discriminator W-Net*: For each lesion segmentation network S_l , we aim to minimize discrepancies between different domain's feature embedding estimated at the encoder layers S_l^e of S_l . To this end, we introduce the domain critic *W-Net* parameterized by θ_w , whose goal is to estimate the Wasserstein distance Arjovsky et al. (2017) between the source

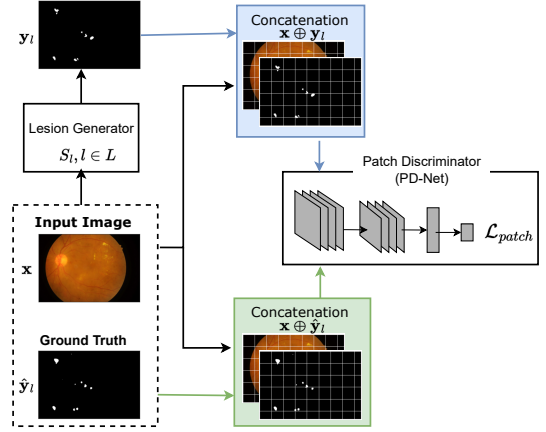


Fig. 3: Our workflow for the supervised lesion segmentation using adversarial learning. Output from the segmentation network S_l is concatenated with the input image and split into patches. Then, the patch discriminator *PD-Net* computes the adversarial loss by predicting whether each patch is real or fake.

and target distribution in the feature representation space (Fig. 4). Given an encoder feature representation $\mathbf{h} = S_l^e(\cdot)$ for an image \mathbf{x} from any domain, we define:

$$\mathbf{h}_s = S_l^e(\mathbf{x}_s), \quad \mathbf{x}_s \in \mathcal{X}_s, \quad (6)$$

$$\mathbf{h}_t = S_l^e(\mathbf{x}_t), \quad \mathbf{x}_t \in \mathcal{X}_t. \quad (7)$$

and the domain critic function $W(\cdot): \mathbb{R}^d \rightarrow \mathbb{R}$ which maps a feature representation to a real number. As proposed by Shen et al. (2018), if the parameterized family of domain critic function $W(\cdot)$ are all 1-Lipschitz, for the source and target distributions \mathcal{X}_s and \mathcal{X}_t , an empirical Wasserstein distance can be approximated by *maximising domain critic loss* \mathcal{L}_{wd} with respect to θ_w :

$$\mathcal{L}_{wd}(\mathcal{X}_s, \mathcal{X}_t) = \frac{1}{|\mathcal{X}_s|} \sum_{\mathbf{x}_s \in \mathcal{X}_s} W(\mathbf{h}_s) - \frac{1}{|\mathcal{X}_t|} \sum_{\mathbf{x}_t \in \mathcal{X}_t} W(\mathbf{h}_t). \quad (8)$$

To make the training progress to be stable, we further enforce parameters θ_w to *minimize the Lipschitz constraint* using gradient penalty \mathcal{L}_{grad} proposed by Gulrajani et al. (2017) of the domain critic as:

$$\mathcal{L}_{grad}(\hat{\mathbf{h}}) = \left(\left\| \nabla_{\hat{\mathbf{h}}} W(\hat{\mathbf{h}}) \right\|_2 - 1 \right)^2, \quad (9)$$

where $\hat{\mathbf{h}} = \{\mathbf{h}_s, \mathbf{h}_t, \mathbf{h}\}$ is the feature representations at which to penalize the gradients and it is defined by the source and target representations $\mathbf{h}_s, \mathbf{h}_t$ as well as at the random points \mathbf{h} along the straight line between source and target representation pairs Shen et al. (2018); Gulrajani et al. (2017).

Combining Eq. (8) and Eq. (9), the optimization problem for the *W-Net* and the lesion attribute segmenter S_l ($l \in L$), which minimizes discrepancy between two domains \mathcal{X}_s and \mathcal{X}_t in terms of Wasserstein distance, is defined as:

$$\mathcal{L}_{wass} = \min_{\theta_{S_l}} \max_{\theta_w} \{ \mathcal{L}_{wd} - \eta \mathcal{L}_{grad} \}, \quad (10)$$

where η is the regularization coefficient.

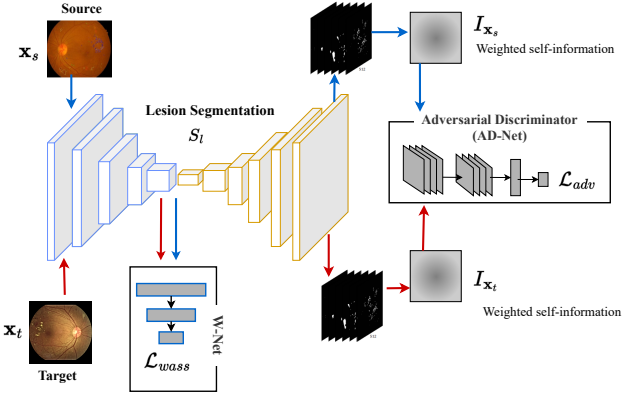


Fig. 4: Domain Adaptation Components in our method with *W-Net* and *AD-Net*. The *W-Net* is designed to minimize the Wasserstein Distance Minimization between two feature embedding spaces in the source and target domain. The *AD-Net* is employed as the discriminate network to distinguish entropy distributions from two domains.

3) *Adversarial Domain Discriminator AD-Net*: In order to exploit the structural consistency between the source and target domain, we employ an entropy loss \mathcal{L}_{ent} to directly minimize an uncertainty prediction Vu et al. (2019); Ma et al. (2021) in the target domain of S_l . Given an input image in the target domain $\mathbf{x}_t \in \mathcal{X}_t$, we compose the Shannon Entropy map Shannon (2001) $\mathbf{E}_{\mathbf{x}_t} \in [0, 1]^{h \times w}$:

$$\mathbf{E}_{\mathbf{x}_t}^{(h,w)} = \frac{-1}{\log(C)} \sum_{i=1}^C P_{\mathbf{x}_t}^{(h,w,i)} \log P_{\mathbf{x}_t}^{(h,w,i)}, \quad (11)$$

at each pixel (h, w) . Here, C being the number of output class, i.e., $C = 2$ in our setting with binary segmentation for each lesion attribute $l \in L$, and $P_{\mathbf{x}_t}^{(h,w,i)}$ is the pixel-wise predicted class score estimated from $S_l(\mathbf{x}_t)$.

We now define an entropy loss \mathcal{L}_{ent} which is the sum of all pixel-wise normalized entropy:

$$\mathcal{L}_{ent}(\mathbf{x}_t) = \sum_{h,w} \mathbf{E}_{\mathbf{x}_t}^{(h,w)} \quad (12)$$

By combining Eq.(1) and Eq. (12), we can jointly optimize the supervised segmentation loss with the samples in the source domain \mathcal{X}_s and an unsupervised entropy loss on the target domain \mathcal{X}_t by:

$$\min_{\theta_{S_l}} \frac{1}{|\mathcal{X}_s|} \sum_{(\mathbf{x}, \mathbf{z}_l) \in \mathcal{X}_s} \mathcal{L}_{wbce}(S_l(\mathbf{x}), \mathbf{z}_l) + \frac{\lambda_{ent}}{|\mathcal{X}_t|} \sum_{\mathbf{x}_t \in \mathcal{X}_t} \mathcal{L}_{ent}(\mathbf{x}_t), \quad (13)$$

with λ_{ent} is the weight factor for the entropy part \mathcal{L}_{ent} .

Training the lesion segmentation model S_l with the joint loss function in Eq.(13) has shown improvement in experiments. However, merely minimization this does not entirely capture the structural dependencies between the local semantics. In other directions, authors in Tsai et al. (2018) have argued that adaptation to the structural output space is favorable for unsupervised domain adaptation in semantic

segmentation tasks. Similarly, Shen et al. (2018) have also shown that adaptation in the latent space can enhance the model generalization ability. These premises are based on the fact that the source and target domain usually share strong similarities in the semantic layout. To exploit such observations, we incorporate an adversarial training framework to implicitly guide the target domain’s entropy distributions to be similar to the source ones Vu et al. (2019); Ma et al. (2021). Our motivation is based on the fact that a trained model naturally produces a high confidence score for one target class and low for the rest on source-like images. Therefore, entropy for the source-like images will be low, and that of target images will be higher.

Using the equation (11), we define a *weighted self-information map* I_x for any input image \mathbf{x} composed of pixel-level vectors at each pixel (h, w) as:

$$I_x^{(h,w)} = -P_x^{(h,w)} \circ \log P_x(h, w) \quad (14)$$

where \circ stands for hadamard product, $P_x^{(h,w)} = [P_x^{(h,w,i)}]_{i=1}^C$ is the probability score for C classes at (h, w) estimated by $S_l(x)$.

Given this, we define $I_{\mathbf{x}_s}$, $I_{\mathbf{x}_t}$ as weighted self-information maps for the source and target domain $\mathcal{X}_s, \mathcal{X}_t$ respectively computed by:

$$I_{\mathbf{x}_s}^{(h,w)} = -P_{\mathbf{x}_s}^{(h,w)} \circ \log P_{\mathbf{x}_s}(h, w) \quad (15)$$

$$I_{\mathbf{x}_t}^{(h,w)} = -P_{\mathbf{x}_t}^{(h,w)} \circ \log P_{\mathbf{x}_t}(h, w) \quad (16)$$

We now formulate the adversarial network *AD-Net* with parameters θ_{ad} as convolutional networks. This network takes I_x as an input and produces domain classification as an output with class label 1/0 for the source/target domain respectively (right side in Fig. 4). Note that, *AD-Net* architecture and its parameters are different from the discriminator network *PD-Net* that we have used to optimised S_l in Eq. (5). Similar to the learning procedure of the original GAN method Goodfellow et al. (2014), the discriminator *AD-Net* is trained to discriminate outputs coming from source and target images and simultaneously, the lesion network S_l is trained to fool the discriminator *AD-Net*. The optimization objective of the discriminator is:

$$\mathcal{L}_{adv} = \min_{\theta_{S_l}} \max_{\theta_{ad}} \frac{1}{|\mathcal{X}_s|} \sum_{\mathbf{x}_s \in \mathcal{X}_s} \log(AD(I_{\mathbf{x}_s})) \quad (17)$$

$$+ \frac{1}{|\mathcal{X}_t|} \sum_{\mathbf{x}_t \in \mathcal{X}_t} \log(1 - AD(I_{\mathbf{x}_t})) \quad (18)$$

In summary, by jointly optimizing equations (5),(10), and (18), we end up with a total loss function:

$$\mathcal{L}_{total} = \mathcal{L}_{seg} + \lambda_p \mathcal{L}_{patch} + \lambda_w \mathcal{L}_{wass} + \lambda_{adv} \mathcal{L}_{adv}. \quad (19)$$

where, λ_p , λ_w and λ_{adv} are the weighting factors for the patch-based adversarial learning, Wasserstein term, and entropy-based adversarial term respectively.

C. Attention-based Classifier

To this end, using lesion segmentation models S_l from the previous step, we generate L distinctive lesion maps $\mathbf{z}_{l=1}^L$ for each input image ξ . The attention module *Attn-Net* then uses this preliminary information to select the most relevant parts contributing toward the better performance of the disease classification network *G-Net*.

This work investigates two different jointly learning frameworks between *Att-Net* and *G-Net* for network architectures based on CNN (section IV-C1) and Transformer (section IV-C3). Furthermore, besides integrating lesion information at a feature level through attention gates, denoted as *low-level concepts* (section IV-C1), we also formulate a novel overlapping constraint among heatmap regions of *G-Net* and segmented multi-lesion regions obtained from *S-Net*, denoted as *high-level concepts* (section IV-C2). Fig. 6 gives an illustration for these attention concepts. In our setting, we develop these constraints for both CNN-based and Transformer-based architectures and discover that they contribute in improving accuracy for several baselines by a large margin (tables VII, VI). Last but not least, these strategies enable an explainable visualization of DR grading predictions when ophthalmologists can observe the correlation of high-responding areas in trained networks with medical priors represented as lesion regions.

1) *Attention Lesion Regions at Low-level Concepts: Attention Network Att-Net and Grading Network G-Net*: Inspired by Zhou et al. (2019), we consider attention mechanisms at feature maps of the classification network *G-Net* given multi-lesion maps predicted by S_l . For this, feature maps at the first and last layers of *G-Net* are jointly combined with lesion maps $\mathbf{z}_{l=1}^L$ to define attention maps that return high responses to different lesion regions characterizing the disease. It is worthy to note that we do not integrate the lesion masks initially predicted by S_l as a direct input for the classification model *G-Net* because the initially predicted masks are usually very tiny and sparse. Their contributions rather than being controlled by the attention network *Att-Net*. In our setting, we choose the ResNet-50 He et al. (2016), including five CNN blocks for the architecture of *G-Net*, and therefore have to modify formulations in Zhou et al. (2019) as follows.

We indicate five CNN blocks of *G-Net* as $G = \{\mathbf{g}^1, \mathbf{g}^2, \mathbf{g}^3, \mathbf{g}^4, \mathbf{g}^5\}$. The feature maps of an image \mathbf{x} at the first block are computed by:

$$\mathbf{f}^{\text{first}} = \mathbf{g}^1(\mathbf{x}) \quad (20)$$

Similarly, the feature maps at the last layer estimated by:

$$\mathbf{f}^{\text{last}} = \mathbf{g}^5(\mathbf{o}^5) \quad (21)$$

where

$$\mathbf{o}^i = \mathbf{g}^{i-1}(\mathbf{o}^{i-1}), \quad i \in [2, 5] \quad (22)$$

$$\mathbf{o}^1 = \mathbf{x} \quad (23)$$

where \mathbf{o}^i indicates the output of each convolutions block.

In the first step, we train *G-Net* with all blocks in a fully supervised manner using the image-level annotations in the target domain $(\mathbf{x}_t, \hat{\mathbf{t}}_t) \in \mathcal{X}_t$. The optimization problem is:

$$\mathcal{L}_{cls} = \min_{\theta_g} \frac{1}{|\mathcal{X}_t|} \sum_{(\mathbf{x}_t, \hat{\mathbf{t}}_t) \in \mathcal{X}_t} \mathcal{L}_{mce}(G(\mathbf{x}_t), \hat{\mathbf{t}}_t), \quad (24)$$

where \mathcal{L}_{mce} is the multi-class cross entropy classification loss defined as:

$$\mathcal{L}_{mce}(\mathbf{t}_t, \hat{\mathbf{t}}_t) = - \sum_{k=1}^C \hat{\mathbf{t}}_t^{(k)} \log \mathbf{t}_t^{(k)} \quad (25)$$

with $\hat{\mathbf{t}}^{(k)}$ is 0 or 1, indicating whether class label k is the correct classification.

Once the model is pre-trained, the feature maps $\mathbf{f}^{\text{first}}$ and \mathbf{f}^{last} are computed using equations (20), (21). Then we define an attentive feature for the l -th lesion y_l obtained from S_l by:

$$\mathbf{f}_l^{\text{first-att}} = \text{ReLU}(\mathbf{W}_l^{\text{first}} \text{concat}(y_l, \mathbf{f}^{\text{first}}) + b_l^{\text{first}}), \quad (26)$$

where $\text{concat}(\cdot)$ is the channel-wise concatenation; $\mathbf{W}_l^{\text{first}}$ and b_l^{first} are additional learnable parameters and bias terms for the l -th lesion.

In a next step, the last feature maps \mathbf{f}^{last} acting as a global feature embedding is correlated with the first-level attentive features to generate attention weights for the l -th lesion:

$$\alpha_l = \text{Sigmoid}(\mathbf{W}_l^{\text{last}} [\mathbf{f}_l^{\text{first-att}} \odot \mathbf{f}^{\text{last}}] + b_l^{\text{last}}), \quad (27)$$

where \odot is the element-wise multiplication; $\mathbf{W}_l^{\text{last}}$ and b_l^{last} are other parameters and bias terms to learn attention features at the global level. To make \mathbf{f}^{last} and $\mathbf{f}_l^{\text{first-att}}$ be compatible in channel dimensions, we also use a 1×1 convolution over the \mathbf{f}^{last} .

By applying Eq.(27) for each lesion $l \in L$, we aggregate all attention lesion maps and use them to separately conduct element-wise multiplication with the first-level features $\mathbf{f}^{\text{first}}$ of *G-Net*. The output feature vectors then are concatenated and utilized as final attention features to fine-tune the DR Grading network *G-Net*. In terms of optimization, parameters of *Att-Net* include $\theta_{Att} = \{(\mathbf{W}_l^{\text{first}}, \mathbf{W}_l^{\text{last}}, b_l^{\text{first}}, b_l^{\text{last}})_{l=1}^L\}$.

Finally we compose an optimization, that jointly learns the grading network *G-Net* and the attention-based lesion *Att-Net* at the *low-level concept* as:

$$\mathcal{L}_{cls}^{\text{att}} = \min_{\theta_g, \theta_{att}} \frac{1}{|\mathcal{X}_t|} \sum_{(\mathbf{x}_t, \hat{\mathbf{t}}_t) \in \mathcal{X}_t} \mathcal{L}_{mce}(G(\mathbf{x}_t) \cdot \text{Att}(S_l(\mathbf{x}_t)_{l=1}^L), \hat{\mathbf{t}}_t). \quad (28)$$

where \mathcal{L}_{mce} is the multi-class cross entropy defined in Eq. (25). We characterize the loss $\mathcal{L}_{cls}^{\text{att}}$ as the low-level concept because it purely combines *G-Net* and *Att-Net* at the feature level through attention weights. While this approach boosts performance, it is still a black box to end-users. In the next section, we introduce a new constraint between two types of networks which are able to enhance accuracy and provide explainable properties for the learned system.

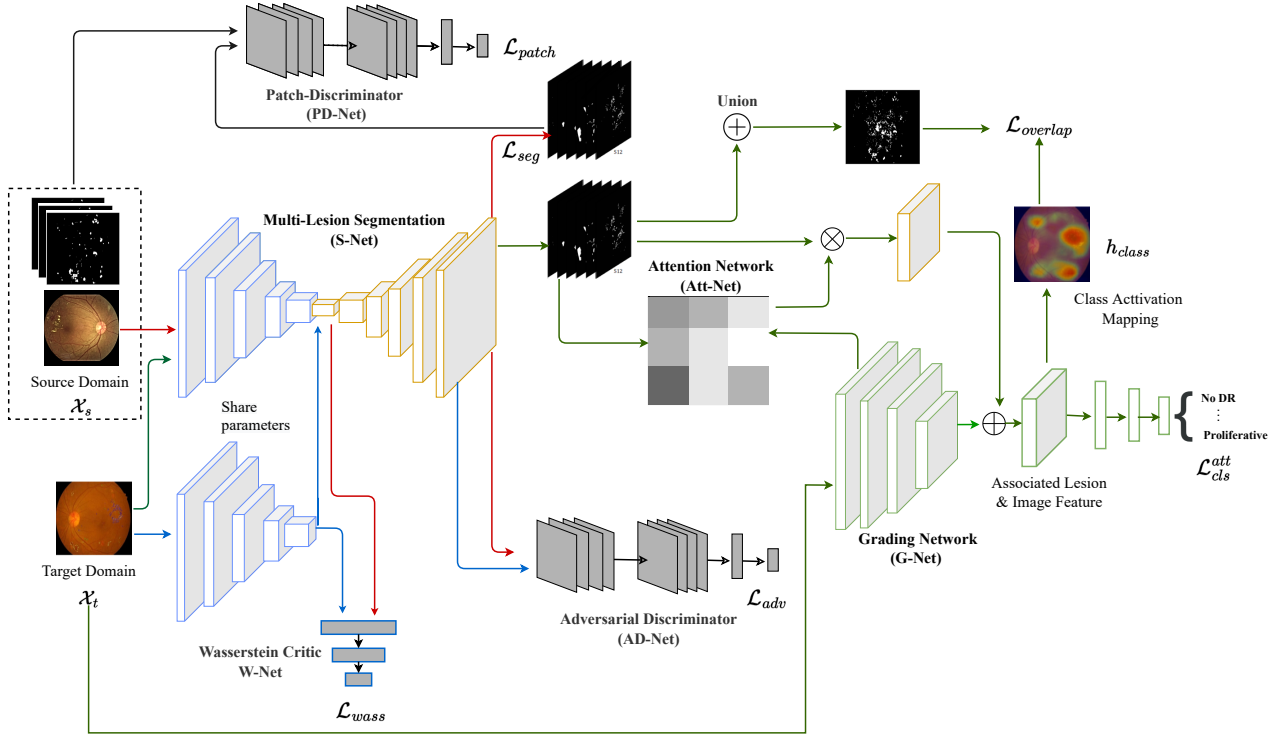


Fig. 5: Detailed architectures and pipeline of the proposed *DRG-AI-System*. It consists of five sub-networks: *S-Net*, *PD-Net*, *AD-Net*, *W-Net*, *Att-Net*, and *G-Net*. These networks are learned in two phases. The first stage aims to train the multi-lesion segmentation networks *S-Net*. To overcome the lack of training data in a source domain and domain adaptation issues in a target domain, *PD-Net*, *W-Net*, and *AD-Net* are jointly integrated. The second stage optimizes the grading network *G-Net* using lesion information obtained from *S-Net*, where the attention network *Att-Net* automatically decides the most influential parts of a given image.

2) *Attention Lesion Regions at High-level Concepts*: The attention procedure that we have used in the previous section is on the structural feature level of the grading network. In this section, we further impose a new constraint that directly compares the class activation map of the grading network with the lesion maps. By considering this property, we explicitly guide the network on which parts of the image they should focus on and make the predictions more transparent to end-users by observing correlations between trained networks' activation map and medical priors (Fig. 15). This sets us apart from prior studies in DR grading problems Zhou et al. (2019); Sun et al. (2021). Below we present the formulation to integrate this constraint seamlessly in our learning framework for the case of *G-Net* based on CNN architecture.

Based on Grad-CAM, we can get the class activation map of the last layer in the grading model *G-Net*. For an input image \mathbf{x} , let $f_{l,k}$ be the activation of unit k in l -th layer. For each of the ground-truth class c , we compute the corresponding gradient score s^c , with respect to activation maps of $f_{l,k}$. These gradient scores then pass through 1×1 convolution of global average pooling layer to obtain the neuron importance weights $w_{l,k}^c$:

$$w_{l,k}^c = \text{GAP} \left(\frac{\partial s^c}{\partial f_{l,k}} \right), \quad (29)$$

where $\text{GAP}(\cdot)$ is the global average pooling. Because $w_{l,k}^c$ indicates the important of activation map $f_{l,k}$ contributing the

prediction of class c , we thus apply the weight matrix w_c as a kernel and apply 2D convolution over the feature map f_l to aggregate all activation maps, followed by a ReLU function to get the activation map AM^c for the c -th class:

$$AM^c = \text{ReLU}(\text{conv}(f_l, w^c)) \quad (30)$$

where l represents the last convolution layer.

In the next step, we normalize the AM^c so that its class channel values are normalized to $[0, 1]$, denoted as \widetilde{AM}^c , using a thresholding operation $T(\cdot)$ Li et al. (2018a) as follows:

$$\widetilde{AM}^c = T(AM^c) \quad (31)$$

$$T(AM^c) = \frac{1}{1 + \exp(-\omega(AM^c - \sigma))} \quad (32)$$

where σ is the threshold matrix whose elements are equal to σ . ω is the scale parameter forcing $T(AM^c)_{i,j}$ approximately equals to 1 if $AM^c_{i,j}$ is greater than σ , or to 0 otherwise.

Finally, we propose an overlapping loss function $\mathcal{L}_{overlap}$ for images whose lesion areas are not empty as:

$$\mathcal{L}_{overlap} = \min_{\theta_g, \theta_{att}} \frac{1}{hw} \|\widetilde{AM}^c - L_U\|_2 \quad (33)$$

where h, w are the height and width of image x , L_U is the union region of all of lesion types computed by:

$$L_U = \bigcup_{l \in L} S_l(x) \quad (34)$$

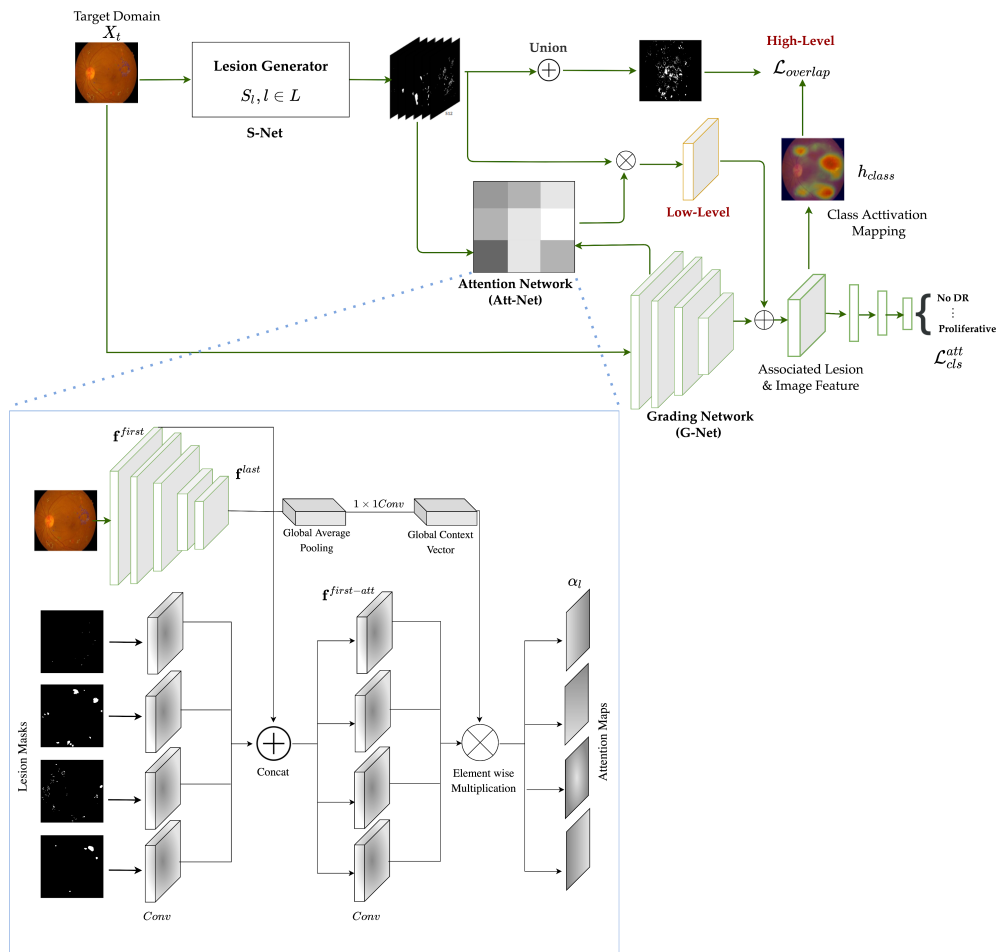


Fig. 6: An overview of our attention mechanisms jointly learning with the DR grading network at both low-level and high-level concepts. In the blue box, internal architecture of low-level attention mechanism is illustrated in detail.

Note that we only compute the $\mathcal{L}_{overlap}$ for an image x if its grading label is different 0, i.e., input image has some stages of DR disease. By optimizing $\mathcal{L}_{overlap}$, we jointly learn parameters for both grading network $G-Net$ and the attentive network $Att-Net$.

Combining equations (33), (28), we end up with a new total object loss function that incorporates attention mechanisms for DR grading task at both low-level and high-level constraints:

$$\mathcal{L}_{grading} = \mathcal{L}_{cls}^{att} + \mathcal{L}_{overlap} \quad (35)$$

At a glance, our proposed loss $\mathcal{L}_{overlap}$ is comparable to existing semi-supervised learning Li et al. (2018a) or Covid-19 detection Wu et al. (2021); however, we extend it for the multi-lesion scenario in the context of the DR grading task. Furthermore, our system is superior to these works and current approaches to the DR problem Zhou et al. (2019); Sun et al. (2021) in that we develop lesion information-based attention mechanisms for classification tasks at both feature-level and high-level concepts, thereby improving performance and providing explainable properties to the entire system (table VI).

3) *Integrating Lesion Features for Transformer-based Methods:* In this section, we investigate the performance of

Transformer architecture for the DR grading task. For this, we choose the MIL-VT method proposed by Yu et al. (2021) (Fig. 7). Compared with ViT, MIL-VT further adds multiple-instance learning heads to leverage the features extracted from individual patches. However, MIL-VT solely employs image-level data in the training stage and ignores the responsibilities of lesion areas. This motivates us to incorporate the MIL-VT attention’s mechanism with our overlapping heatmap concepts presented in section IV-C2. To establish such a constraint, we apply the Attention Rollout technique Abnar and Zuidema (2020); Dosovitskiy et al. (2021) to compute the heatmap regions for MIL-VT.

In particular, Attention rollout is a concept used to track the information propagated from the input layer to the embeddings in the higher layers. Given a Transformer with N layers, in each layer $n \in N$, this technique takes the average of all attention weights across all heads to form an attention matrix A_n where $(A_{ij})_l$ defines how much attention is going to flow from token j in the layer $n - 1$ to token i in the layer n . Then the attention rollout matrix at layer n , denoted as \tilde{A}_n , is computed in a recursive way:

$$\tilde{A}_n = (A_n + I) \tilde{A}_{n-1} \quad (36)$$

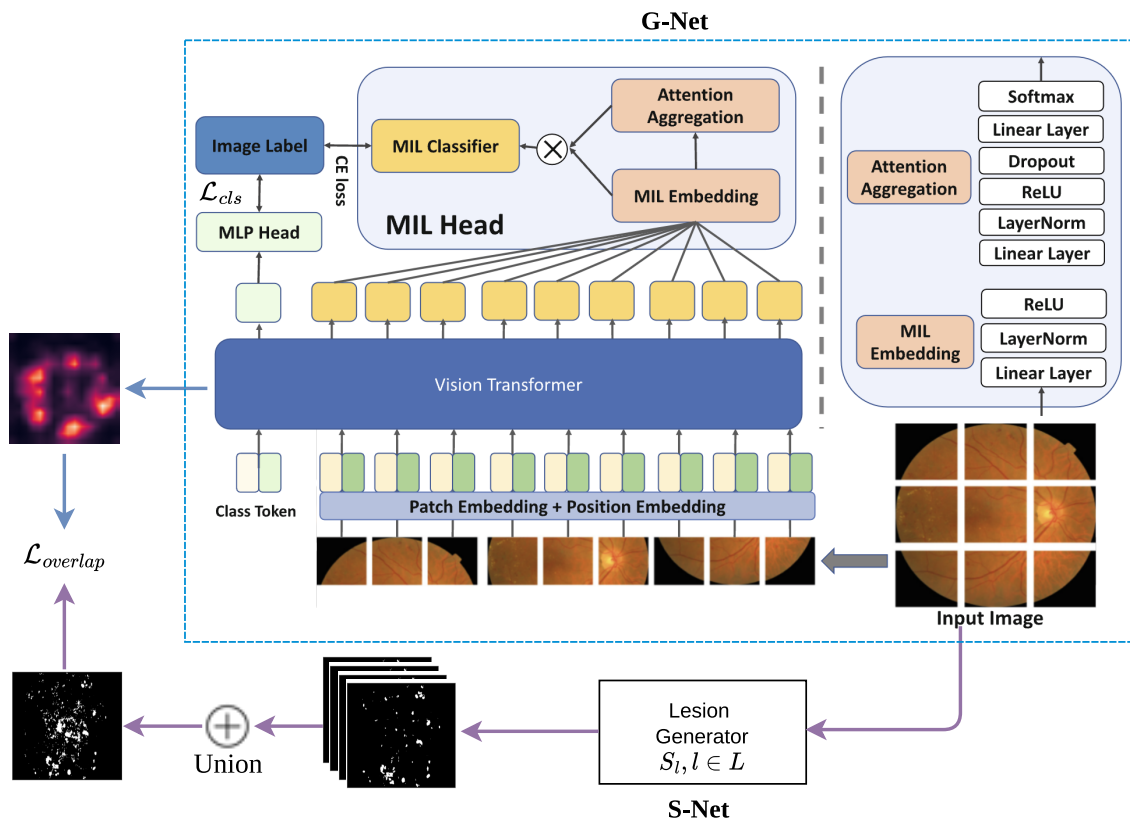


Fig. 7: Our proposed DR-grading transformer architecture. We integrate predicted lesion feature maps using lesion generator S_l for an image with the multi-head lesion generator G -Net based on MIT-VT Yu et al. (2021). We compute $\mathcal{L}_{overlap}$ and the grading model is trained using both \mathcal{L}_{cls} and $\mathcal{L}_{overlap}$.

where I is the identity matrix.

By computing equation 36 at the last layer N , we can account for the combination of attention across tokens through all layers. In our method, we choose the attention map AM^c as:

$$AM^c = \tilde{A}_N. \quad (37)$$

Then the loss $\mathcal{L}_{overlap}$ in equation 33 is defined in analogous way (Fig. 7). In experiment, we discover that this extended version significantly enhances MIL-VT's performance in a variety of situations (table VII).

V. DRG-NET: ARG-EXPERT-INTERACTION

As a joint disease diagnosis system, given a retina fundus image, the system can automatically detect the associated lesion attributes and predict its disease grade. In addition, the detected lesion masks from the segmentation module can support the disease grading prediction by the grading module. Unlike most of the medical decision support systems (Sonntag et al., 2020; Mehta et al., 2018; Dai et al., 2021) where the lesion maps and disease grading predictions modules are independent of each other, our architecture is trained to learn these tasks collaboratively. In the learning phase of our grading model, we exploit predicted lesion information. Besides, the system also facilitates the utilization of expert feedback throughout the training process. Generally, our diagnosis system provides

an interactive way with the expert user, as shown in Fig. 8. For this, the method can deliver a visual explanation to the user about its predictions and incorporate user feedback to fine-tune the model. More details are as follows,

A. DR Grading Predictions with Explainable Properties

Our method focuses on the local interpretability Saini and Prasad (2021); Selvaraju et al. (2017) of our prediction model, which is computed based on the class activation map AM^c . This gives us the discriminative regions used by the model to predict the disease grade for a certain class. By drawing the AM^c over input image x (Fig. 8 - *Visual Explanation*), we can observe the highlighted region on the input x , which the grading network G -Net thought to be the most essential region for its decision (Fig. 8 - *Predicted DR Grade*). Moreover, detected lesion maps can be used as visual explanations. In particular, considering the overlapping region between lesion maps $\hat{z}_{l=1_l}$ (Fig. 8 - *Predicted Lesion Regions*) with activation maps AM^c of x gives a visual interpretation of how much these lesions influenced the grading model prediction (Fig. 8).

B. Improving System's Performance through User Feedback

Getting user feedback can be costly and time-consuming in the medical domain. For instance, lesion regions in diabetic disease can be so tiny that each region covers only a small group of pixels in the image. Our framework alleviates this

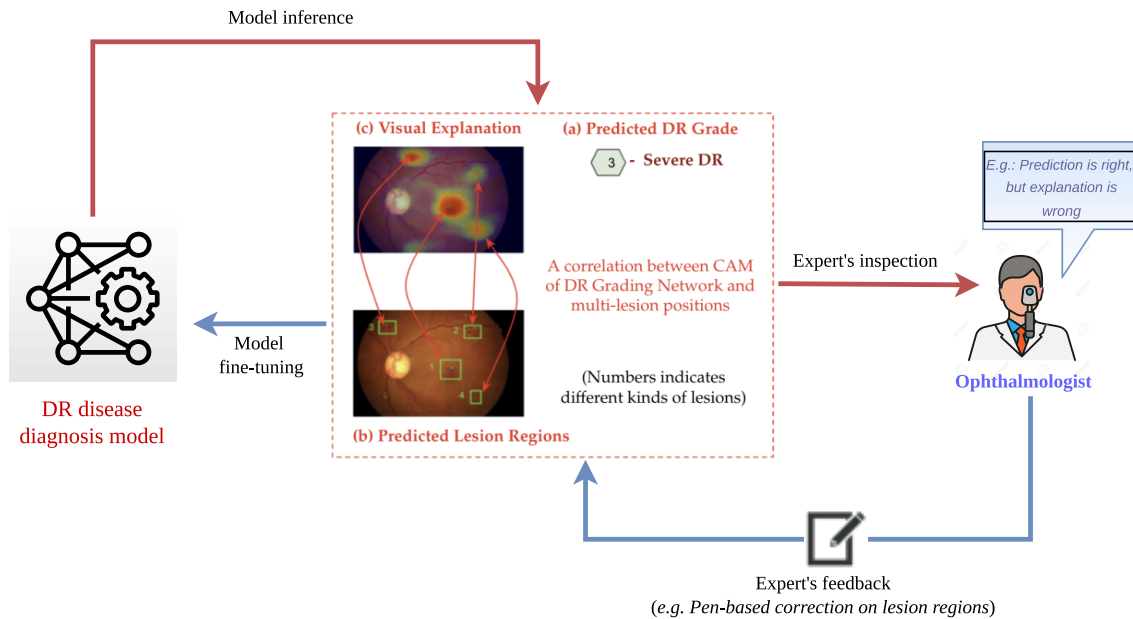


Fig. 8: Illustration for the interaction between experts and the trained model. The model can infer explanatory predictions via presenting disease grade, related lesions, and class activation mapping. Upon inspection, the expert validates the results and, if necessary, provides input (e.g., drawing bounding box on missing lesion regions). This input is used to improve model performance in subsequent model retraining.

issue by not requiring pixel-level training data in the target domain to train segmentation models. It instead is handled by the domain adaptive networks as the Wasserstein network *W-Net* (Section IV-B2) and the Adversarial Discriminator-based on Entropy *AD-Net* (Section IV-B3). Given this, we can generate different lesion regions while only using pixel-level labels from another source domain.

When the system is deployed in practice, the expert can provide two feedback forms. Firstly, given new annotations on lesion masks, we can fine-tune our lesion generator models *S-Net*. Specifically, for each lesion generator model S_l , we update the segmentation model using *new labeled data in the target domain* by training:

$$\mathcal{L}_{seg} = \min_{\theta_{S_l}} \frac{1}{|\mathcal{X}_t|} \sum_{(\mathbf{x}, z_l) \in \mathcal{X}_t} \mathcal{L}_{wbce}(S_l(\mathbf{x}), \hat{y}_l) \quad (38)$$

where \mathcal{L}_{wbce} is the weighted binary cross-entropy loss defined in equation (2). Note that in this case, we can ignore the domain adaptation parts, which are already optimized during training with data in the source domain X_s .

Secondly, when users provide both new image grading and lesion segmentation labels, we can update either:

- Segmentation models *S-Net* using \mathcal{L}_{seg} in equation (38).
- Attention-based disease grading model *Att-Net* and *G-Net* by learning the objective function $\mathcal{L}_{grading}$ defined in equation (35).

It is worth noting that our technique automatically learns to identify critical lesion locations influencing the DR Grading task by utilizing attention mechanisms; hence, it can be resilient to a certain degree of noise in segmentation annotations provided by experts. In other words, rather than a precise segmentation mask, the expert can mark the region of interest

in the form of bounding boxes or circles around the lesion locations using any pen-based input device. As the attention model inherently learns to filter out the noise and focus on the area of interest, our experiments confirm that only these soft annotations are sufficient to boost the performance of the model (table IX).

VI. EXPERIMENTAL RESULTS

A. Datasets

Retina images are generally captured in two forms, which are Optical Coherence Tomography (OCT) capturing a cross-sectional images of retina and Color Fundus retinal photography capturing 3D retina images using fundus cameras. We employed datasets with the later one for all our experiments in this work. For domain-invariant lesion attributes segmentation, we used two publicly available datasets. To the best of our knowledge, these two are the only datasets that provide pixel-level annotations for diabetic retinopathy. The datasets are:

- *IDRID segmentation* Porwal et al. (2018): This dataset contains 81 high resolution (4288×2800 pixels) images with four different types of lesion annotations and is split into 54 training images and 27 testing images. The lesions are: microaneurysms (MA), haemorrhages (HE), hard exudates (EX) and soft exudates (SE). Each of these lesions are annotated in the forms of binary masks.
- *FGADR segmentation* Zhou et al. (2020): Similarly as IDRID, this dataset contains 1843 images with 4 kinds of lesion masks (MA, HE, EX, and SE). The training set consists of 1500 images and the remaining 343 images are for test set. This dataset has imbalance in the lesion classes. The class HE is available in 1471 images which is

78% of the total images where the class MA is available for only 610 images which consists of 33% of the total images.

For the classification task, we used three publicly available datasets.

- *IDRID classification* Porwal et al. (2018): This dataset consists of 413 training and 103 test images with 5 severity grading labels. The five labels include: *normal, mild, moderate, severe and proliferative*, which are annotated as 0, 1, 2, 3, 4, respectively. These images only have image-level labels and do not have any pixel-level lesion masks annotations.
- *EyePACS* EyePACS (2015): This dataset consists of 35,126 training images and 53,576 testing images with similar grading protocol of classes with 5 categories. Images in this dataset is captured using different types of cameras settings under various light conditions.
- *FGADR classification* Zhou et al. (2020): this dataset consists of 1500 training images and 343 testing image for diabetic retinopathy grading. This is the only one that contains both image-level pixel disease grading and pixel-level lesion annotation maps.

Figure 9 shows the class distribution for the three classification datasets we used in our work. We can observe that there are great numbers of class imbalance in all three datasets.

B. Evaluation Metric

To evaluate the segmentation performance of multi-lesion segmentation, we used two common metrics i.e., Area Under the Curve of Receiver Operating Characteristics (AUC-ROC) and Area Under the Curve of Precision-Recall (AUC-PR). The positive class means the existence of lesion and negative is the otherwise. For evaluating multi-class disease grading classification task, we used Accuracy and Quadratic Weighted Kappa (Kappa). Detailed definitions of these measures are as follows:

- *AUC-ROC* measures the class separability at various threshold settings. ROC is the probability curve and AUC represents the degree of measures of separability. It compares true positive rate (sensitivity/recall) versus the false positive rate (1 - specificity). The higher the AUC-ROC, the bigger the distinction between the true positive and false negative.
- *AUC-PR*: It combines the precision and recall, for various threshold values, it compares the positively predicted value (precision) vs the true positive rate (recall). Both precision and recall focus on the positive class (the lesion) and unconcerned about the true negative (not a lesion, which is the majority class). Thus, for class imbalance, PR is more suitable than ROC. The higher the AUC-PR, the better the model performance.
- *Accuracy*: The normal classification accuracy which simply measures how many observations are correctly classified.
- *Quadratic Weighted Kappa (Kappa)*: It is similar to the Cohen’s kappa metric McHugh (2012) by the weights are set to ‘Quadratic’. Cohen’s kappa measures the agreement

between two raters who each classify N number of items into C mutually exclusive categories. The formulation is:

$$\text{kappa} = \frac{p_o - p_e}{1 - p_e}, \quad (39)$$

where p_o denotes the relative observed agreement between the raters and p_e is the hypothetical probability of chance agreement.

C. Implementation Details

We implemented all experiments using PyTorch framework Paszke et al. (2019) and executed on a computer 2 NVIDIA TITAN RTX 24GB GPUs. For all experiments, the sizes of the input images are 512×512 .

1) *Domain Invariant Lesion Attribute Learning*: For the experiments in lesion attribute segmentation discussed in section IV-A, we used pixel values in the range [0, 1] for retina images and ground-truth binary lesion segmentation masks. In this step, the input image are labeled images from source domain and unlabeled images for the target domain. We applied preprocessing steps as proposed in Xiao et al. (2019) and data augmentation for input images.

Our *S-Net* model described in section IV-A is a U-shaped Ronneberger et al. (2015) encoder-decoder segmentation network. The encoder architecture is identical to the convolutional block of the ResNet50 He et al. (2016) model and the decoder architecture is up-scaled accordingly. The architecture of the *PD-Net* described in section IV-B1 is similar to the InfoGAN Chen et al. (2016). This discriminator model provides stable performance for our case. It consists of two convolution layers with 64 and 128 kernels, respectively, followed by two fully-connected layer of 1024 dimensions and then the sigmoid layer.

For training the *PD-net* IV-B1, we used SGD with momentum Liu and Belkin (2018) as optimizer with initial learning rate of 10^{-4} and momentum value of 0.9. We adopted the cyclic learning scheduler Smith (2017) with max value of 10^{-2} . The class balancing hyper-parameter weight β for the segmentation loss \mathcal{L}_{wbce} described in equation 2 is set to 10 following Xiao et al. (2019) to address class imbalance for lesion and non-lesion class. The value of λ_p for the source domain adversarial joint optimization in equation (5) is set to 10^{-2} . For domain adaptation fine-tuning training, pretrained *S-Net* from IV-B1 is trained with Wasserstein critic model *W-Net* (section IV-B2) and entropy-based discriminatory network *AD-Net*. *W-Net* is a fully connected neural network which takes 1D encoder block outputs from *S-Net* as inputs. *W-Net* has two fully connected layers with number of neurons of 128 and 64, respectively, and final output is linear layer which gives a single scalar value, the critic score. *AD-Net* architecture is adopted from Vu et al. (2019) which have five convolutional layers. The input for *AD-Net* is the weighted self-information maps computed on the output of *S-Net* using equation (16) and output is the binary class probability score on input being source or target domain.

For training both *W-Net* and *AD-Net*, we used Adam optimizer with a learning rate 10^{-4} . The optimizer hyper-parameters for *S-Net* in this step are kept unchanged and they

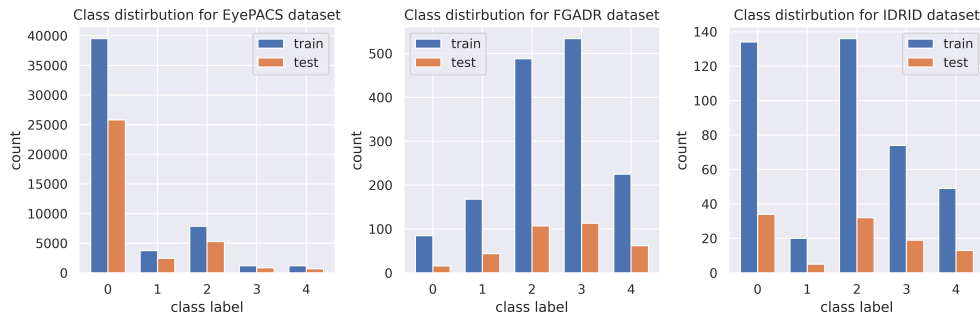


Fig. 9: Class distributions in the three classification datasets used in our work.

are similar to the one discuss in the previous step. Following Vu et al. (2019), the weight factor λ_{ent} in Eq. (13) and λ_{adv} in Eq. (19) are 10^{-3} . We used batch size of 8 for our experiments.

2) *Lesion Attentive Grading Model*: To train the lesion attentive grading models *G-Net* and *Att-Net*, we followed the similar pre-processing and augmentation steps for the input images as with the grading model.

The backbone of our lesion attentive grading model is a ResNet50 He et al. (2016) architecture with the output fully connected layer modified to predict five classes. The attention module *Att-Net* consists of multiple convolutional layers. This network is optimized using Eq. (35) using the cross-entropy loss. As we can see from figure 9, there is a significant class imbalance among different types of lesions across all datasets, we thus compute class-weight for each lesion attribute during the optimization step. We used the SGD optimizer Ruder (2016) with initial learning rate 10^{-3} and applied the cyclic learning strategy as in lesion segmentation steps. For all the experiments, we varied the batch size between 16 and 32. For all of our experiments we have used 10% of training data as validation set and final results are computed on test set.

D. Performance of Multi-Lesion Segmentation Task

1) *Influence of Pre-training Steps on Lesion Generator Models*: As discussed in section IV-A, our lesion segmentation model *S-Net* is firstly pre-trained using the lesion segmentation labels from the source domain data in a fully supervised manner. To evaluate the effectiveness of task agnostic transfer learning (TATL) (Nguyen et al. (2022b)) and the adversarial learning (*PD-Net*) during the pre-training step, we test with three settings:

- *S-Net*: Lesion feature generator segmentation model (*S-Net*) is trained only using the segmentation loss \mathcal{L}_{seg} in equation 1. We do not adapt either TATL strategy or adversarial trainings.
- *S-Net* + *PD-Net*: We incorporate adversarial learning strategy on source domain as discussed in section IV-B1. We jointly the *PD-Net* with *S-Net* segmentation model by optimization the formula in equation 5.
- *S-Net* + *PD-Net* + TATL: We apply both *task agnostic transfer learning (TATL)* and adversarial learning with *PD-Net* to learn *S-Net* using data from the source domain.

Table II and III compare the results of different settings for *IDRID* and *FGADR* segmentation datasets respectively. The segmentation performance is evaluated by AUC-ROC and AUC-PR values on four different lesions, including microaneurysms (MA), haemorrhages (HE), hard exudates (EX) and soft exudates (SE). For *IDRID-segmentation* dataset in table II, we can observe slight improvement in performance for settings *S-Net* + *PD-Net* compared with original *S-Net* settings. With the combinations of TATL in settings *S-Net* + *PD-Net* + TATL, we observe significant improvements in results for all of the lesion classes. For instance, comparing with *S-Net* settings, we gained 2.5% and 5.5% on AUC-ROC and AUC-PR scores respectively, averaged over all four lesions. For the lesion class *HE*, our method achieved highest improvement in AUC-PR scores of 9.4%.

We can observe the similar trend in results on the test set of *FGADR-segmentation* dataset in table III. There is an improvement of 8.5% in the AUC-PR scores averaged over all four lesion classes. To summarize from the results, we conclude that combining adversarial training using the *PD-Net* and the TATL strategy provided a better pre-training performance for *S-Net* in the source domain supervised learning.

2) *Influence of Domain Adaption on Lesion Generator Models*: In this section, we present the results of our domain adaption approaches in different settings and compare with different methods. As discussed in section IV-B, the aim of domain adaptation is to train a neural network using available labeled data from source domain and secure a good accuracy on target domain. We evaluated our approach on *IDRID* and *FGADR* datasets in the forms of *source* \rightarrow *target*:

- *IDRID* \rightarrow *FGADR*: evaluation on *FGADR-segmentation* test set when domain adaptive segmentation model is trained using the *labeled* data from *IDRID-segmentation* dataset and *unlabeled* images from *FGADR-segmentation* dataset.
- *FGADR* \rightarrow *IDRID*: evaluation on *IDRID-segmentation* test set when domain adaptive segmentation model is trained using the *labeled* data from *FGADR-segmentation* dataset and *unlabeled* images from *IDRID-segmentation* dataset.

We report the results for domain adaptation on tables IV and V. Our domain adaption approach discussed in section IV-B

TABLE II: Contributions of task agnostic transfer learning TATL and Adversarial training PD-Net (section IV-B1) in learning lesion segmentation model S-Net in the source domain. Results are evaluated using the training and testing set of *IDRID segmentation*.

Methods	MA		HE		EX		SE	
	ROC	PR	ROC	PR	ROC	PR	ROC	PR
S-Net	0.937	0.440	0.896	0.459	0.931	0.722	0.953	0.583
S-Net + PD-Net	0.932	0.439	0.917	0.481	0.946	0.735	0.965	0.611
S-Net+PD-Net+TATL	0.953	0.456	0.931	0.553	0.961	0.772	0.970	0.643

TABLE III: Contributions of task agnostic transfer learning TATL (Nguyen et al. (2022b)) and Adversarial training PD-Net (section IV-B1) in learning lesion segmentation model S-Net in the source domain. Results are evaluated using the training and testing set of *FGADR segmentation*.

Methods	MA		HE		EX		SE	
	ROC	PR	ROC	PR	ROC	PR	ROC	PR
S-Net	0.901	0.373	0.941	0.611	0.947	0.602	0.927	0.410
S-Net + PD-Net	0.926	0.394	0.955	0.638	0.959	0.667	0.941	0.492
S-Net+PD-Net+TATL	0.937	0.417	0.963	0.652	0.970	0.714	0.954	0.553

TABLE IV: *IDRID* \rightarrow *FGADR*: Semantic segmentation performance on *FGADR* (*target domain*). Models are trained with labeled data on *IDRID* and increasingly labeled data in the target domain from 0 \rightarrow 100%. **Red** indicates the best results for settings using 0% labeled data from target domain in the training step. **Green** stands for settings using 40% – 60% labeled data in target domain but outperform at least one of the methods trained with 100% data. **Bold** are the best values in all methods.

Target Domain	Methods	MA		HE		EX		SE	
		ROC	PR	ROC	PR	ROC	PR	ROC	PR
0%	S-Net	0.752	0.243	0.796	0.280	0.794	0.311	0.728	0.264
	S-Net + Entropy	0.807	0.313	0.843	0.357	0.855	0.407	0.819	0.341
	S-Net + AD-Net	0.841	0.348	0.903	0.448	0.917	0.473	0.902	0.443
	S-Net+AD-Net+W-Net	0.894	0.357	0.911	0.502	0.939	0.538	0.915	0.522
40%	S-Net+AD-Net+W-Net	0.938	0.411	0.953	0.613	0.966	0.682	0.965	0.634
60%	S-Net+AD-Net+W-Net	0.946	0.438	0.969	0.648	0.979	0.728	0.971	0.655
80%	S-Net+AD-Net+W-Net	0.954	0.458	0.973	0.671	0.981	0.732	0.977	0.684
100%	S-Net+AD-Net+W-Net	0.958	0.462	0.979	0.676	0.990	0.739	0.984	0.693
100%	FCN-8s Zhou et al. (2020)	0.925	0.363	0.962	0.606	0.981	0.686	0.963	0.642
	U-Net Zhou et al. (2020)	0.927	0.382	0.967	0.643	0.982	0.726	0.977	0.683
	DL-V3+ Zhou et al. (2020)	0.934	0.364	0.973	0.619	0.981	0.708	0.967	0.659
	Attention U-Net Zhou et al. (2020)	0.942	0.435	0.974	0.678	0.984	0.731	0.980	0.685

consists of modules for Adversarial Entropy Minimization and Wasserstein based distance minimization between source and target domain. To evaluate the effectiveness of different constraints for our domain adaptive segmentation model, we considered four experiments settings:

- 1) **S-Net**: The baseline approach for our domain adaptation approaches. *S-Net* is trained on source domain by adopting the pre-training method including PD-Net and TATL. This model is trained using only the equation 5. Neither domain adaptation constraints are considered.
- 2) **S-Net + Entropy**: We apply direct entropy minimization constraint for target domain in the learning process of *S-Net* as discussed in section IV-A. The entropy loss \mathcal{L}_{ent} in equation (12) is used for minimization on the unlabeled data from target domain and model is optimized with the segmentation loss \mathcal{L}_{seg} using equation (13).
- 3) **S-Net + AD-Net**: Instead of using direct entropy minimization \mathcal{L}_{ent} , we use the proposed domain adaptation with minimizing entropy-based adversarial learning *AD-Net*. *S-Net* and *AD-Net* are optimized together by combining adversarial loss \mathcal{L}_{adv} in equation (18) with \mathcal{L}_{seg} in equation (13).
- 4) **S-Net + AD-Net + W-Net**: Additional domain critic *W-Net* is added along with *S-Net* and *AD-Net* to minimize the domain gap in feature representation using Wasserstein loss \mathcal{L}_{wass} . This is our proposed setting

where all modules are jointly trained using our optimization problem in equation (19).

a) **Results on *IDRID* \rightarrow *FGADR***:: In table IV, we report the results for different settings on *FGADR segmentation* test set. These models are trained using the labeled data from *IDRID* training dataset and unlabeled data from *FGADR* dataset. We can observe that the settings without any domain adaptation *S-Net* performed poorly during the inference on *FGADR* domain. The AUC-PR scores for all of the lesion classes are below 0.3. Direct entropy minimization method (S-Net + Entropy) has significant improvement in both the metrics with respect to S-Net. Introducing Adversarial network for entropy minimization (S-Net + AD-Net) has improved the AUC-ROC and AUC-PR scores by 12% and 15.3%, respectively, averaged over all four lesion classes. The best results among our domain adaptive settings with 0% labeled data in target domain are highlighted in red. In short, we achieved the best results for all of the lesion classes when both adversarial entropy minimization and Wasserstein domain critic model are considered together.

Plots in figure 10 compare the improvement in AUC-PR scores on the lesion classes of *FGADR segmentation* test set for different domain adaptation settings. In summary, we observe that all of our domain adaptive settings contribute for significantly improving performance over non-adaptive settings S-Net. Besides, it can be seen in figure 11 that the training and validation loss curves of all lesion classes for

TABLE V: $FGADR \rightarrow IDRID$: Semantic segmentation performance on $IDRID$ (target domain). Models are trained with labeled data on $FGADR$ and increasingly labeled data in the target domain from $0 \rightarrow 100\%$. **Red** indicates the best results for settings using 0% labeled data from target domain in the training step. **Green** stands for settings using 40% – 60% labeled data in target domain but outperform at least one of baselines trained with 100% data. **Bold** are the best values in all methods.

Target Domain	Methods	MA		HE		EX		SE	
		ROC	PR	ROC	PR	ROC	PR	ROC	PR
0%	S-Net	0.813	0.232	0.803	0.251	0.837	0.363	0.783	0.241
	S-Net + Entropy	0.884	0.331	0.874	0.375	0.902	0.531	0.865	0.404
	S-Net + AD-Net	0.925	0.408	0.902	0.447	0.911	0.697	0.879	0.447
	S-Net+AD-Net+W-Net	0.947	0.436	0.911	0.462	0.927	0.772	0.890	0.476
40%	S-Net+AD-Net+W-Net	0.971	0.483	0.957	0.631	0.946	0.829	0.937	0.634
60%	S-Net+AD-Net+W-Net	0.983	0.502	0.968	0.658	0.969	0.841	0.943	0.669
80%	S-Net+AD-Net+W-Net	0.985	0.510	0.979	0.682	0.977	0.847	0.959	0.710
100%	S-Net+AD-Net+W-Net	0.988	0.511	0.982	0.700	0.978	0.851	0.961	0.714
100%	Adv. HEDNet Xiao et al. (2019)	-	0.439	-	0.483	-	0.840	-	0.481
	AdvSeg Hung et al. (2018)	0.961	0.470	0.924	0.592	0.945	0.79	0.939	0.675
	ASDNet Zhou et al. (2019)	0.969	0.478	0.932	0.628	0.950	0.809	0.948	0.692
	CoLL Zhou et al. (2019)	0.965	0.473	0.954	0.657	0.967	0.845	0.953	0.716

the setting S-Net + AD-Net + W-Net using 0% labeled data from the $FGADR$ monotonously decline, confirming the stability in the learning process.

In table IV, we compare our method with several state-of-the-art techniques: Fully convolutional segmentation ($FCN-8s$) Long et al. (2015), Deep Lap model ($DLV3+$)Chen et al. (2017), U-shaped models ($U-Net$) Ronneberger et al. (2015), and *Attention U-Net* Islam et al. (2019)) using the results reported in Zhou et al. (2020). The training are conducted directly on the target domain $FGADR$ using 100% training labels. For a detailed comparison, we trained our domain adaptive model along with different percentages of labeled data from target domain. Results in green indicate the settings where we surpassed one or more methods under comparison while using 40% \rightarrow 60% labeled data. Results in bold indicate the best scores in all settings. In general, we observe that, for all of the lesion classes, by using only 40% – 60% of labeled data in the target domain, we are able to outperform more than one baselines and with 80% – 100% labeled data, we derive better AUC-ROC and AUC-PR scores compared with other methods in most cases. For instance, we gained 1.6%, 0.5%, 0.6% and 0.4% AUC-ROC score improvement on MA , HE , EX , and SE lesion classes respectively. The AUC-PR scores also improved for MA , EX and SE by 2.7%, 0.8% and 1.2% respectively. Figure 12 illustrates qualitative comparisons of lesion map predictions between S-Net settings and our proposed multi-lesion segmentation model trained with domain adaption constraints S-Net + AD-Net + W-Net.

b) *Results on $FGADR \rightarrow IDRID$* : Table V shows the results on four lesion classes on $IDRID$ -segmentation test set where the segmentation model is trained using the labeled data from $FGADR$ -segmentation set and unlabeled images from $IDRID$ -segmentation training dataset. For different domain adaption settings, we discover similar trends as the $IDRID \rightarrow FGADR$ case. In particular, we compare our method with the following state-of-the-art techniques: adversarial learning based segmentation networks *Adv. HEDNet* Xiao et al. (2019), *AdvSeg* Hung et al. (2018) and semi-supervised collaborative learning networks *ASDNet* and *CoLL* Zhou et al. (2019). The training is conducted with 100% labeled instances in the target domain ($IDRID$). With 0% of label data, the configuration S-Net + AD-Net + W-Net already has comparable per-

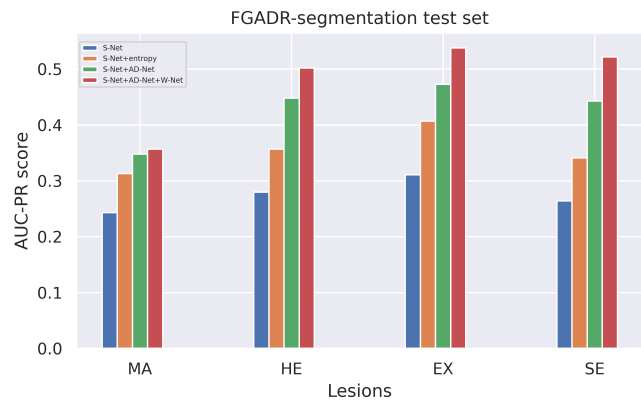


Fig. 10: Comparison of our different domain adaption approaches for lesion segmentation on four types of lesions. Results are evaluated on the setting $IDRID \rightarrow FGADR$ with 0% in target domain.

formance with the first baseline *Adv. HEDNet*. When using 40% labeled data, we are able to outperform most of competitive baselines in both AUC-ROC and AUC-PR metrics. This shows that, the proposed lesion generator model can be fine-tuned with minimal annotation data while still attains good performance in the target domain.

E. Performance of Diabetic Grading Tasks with Attentive Lesion Information

1) Influence of Attention Mechanism on Grading Networks:

We evaluated the effectiveness of predicted lesion segmentation maps in disease grading classification tasks. Our evaluation is on two types of vision related foundation models: CNN-based architecture and Vision Transformer-based architecture. We conducted experiments with the following settings.

- 1) *G-Net*: In this baseline, we directly train the disease grading classification network using retina fundus images and their associated disease grading labels using the classification loss \mathcal{L}_{cls} in equation (24). In this step only *G-Net* is trained and no attention functionality is used, therefore, we do not use any lesion information in the training process.

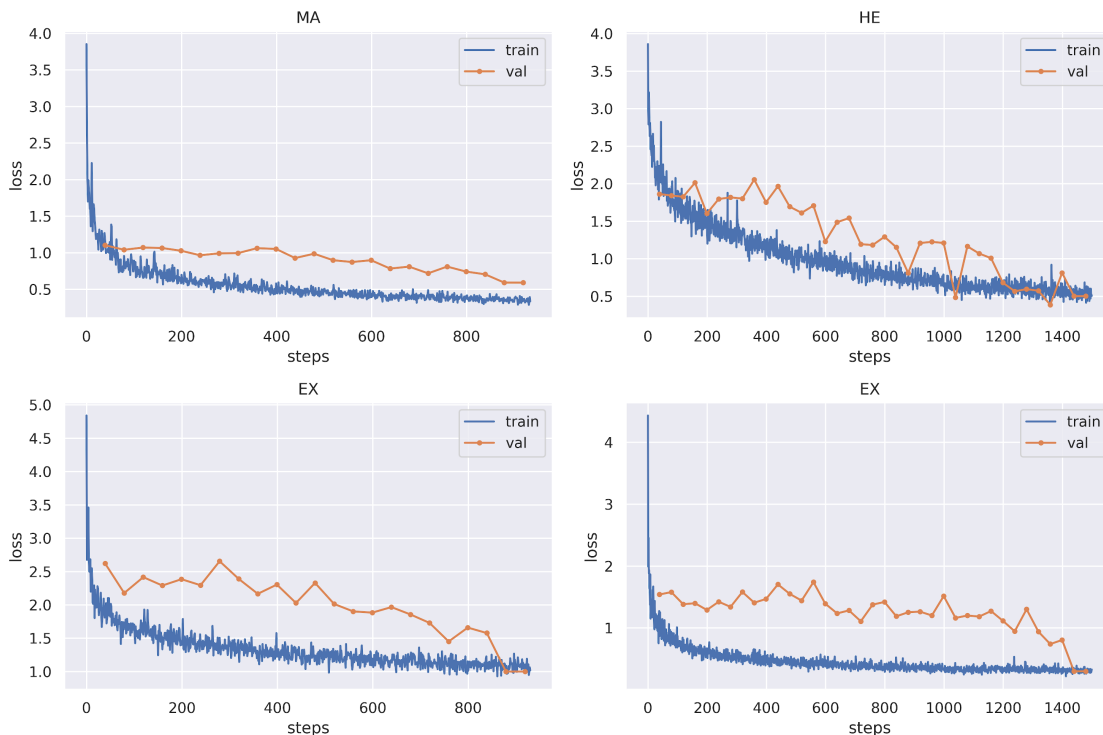


Fig. 11: Training and validation loss curves for our domain adaptive lesion segmentation models. Results are on the setting $IDRID \rightarrow FGADR$ with 0% labeled data in the target domain. It can be seen that all training and validation curves tend to converge to stable points given more training steps.

- 2) G-Net + Attention (low-level): We integrate an attention model *Att-Net* to highlight generated lesion features in the training process of the grading network *G-Net*. The attention mechanism we integrated here is on structural feature level of the grading network described in section IV-C1. Here, the *G-Net* and *Att-Net* are jointly trained using equation (28).
- 3) G-Net + Attention (high-level): In this setting, we integrate the attention mechanism for lesion features following our high-level concept described in section IV-C2. Unlike the previous low-level concept, this attention constraint is more intuitive where the normalized class activation maps are directly compared with the lesion feature maps to compute the attention overlapping loss $\mathcal{L}_{overlap}$ in equation (33). The *G-Net* and *Att-Net* then are jointly trained for classification.
- 4) G-Net + Attention (two-level): We combine both of the proposed *low-level* and *high-level* attention concept in the training process of the disease grading network *G-Net*. This is our final proposed method for the lesion attentive DR grading model. The *G-Net* and *Att-Net* are jointly optimized using the equation (35).

For the CNN-based architecture, we evaluated all four of our proposed settings using *ResNet-50* for the *G-Net* model. For transformer-based architecture, we considered multi-head vision transformer (*MIL-Vit*) Yu et al. (2021) as *G-Net*. Transformer models are inherently built on attention modules at the structural level (low-level); therefore, we only test G-Net

and G-Net + Attention (high-level) methods for the transformer architecture.

We tested our approach on the *IDRID*, *EyePACS* and *FGADR* DR grading datasets. Table VI and VII present the evaluation results for different settings on these datasets for CNN-based and Transformer-based models respectively. For CNN-based models in table VI, we observe that both low-level and high-level attention mechanisms improved the performance for the original classification network G-Net. Integrating low-level attention with grading network in settings G-Net + Attention (low-level), we could increase in Kappa scores by 6%, 5% and 10% for *IDRID*, *EyePACS* and *FGADR* datasets respectively. For the G-Net + Attention (high-level), the kappa scores are improved by 3%, 3% and 7% respectively. We also gained best performance (in bold) for each of the datasets when combining both low-level and high-level attention mechanisms for the setting G-Net + Attention (two-level). Figure 13 describes the comparison between training and validation accuracy in terms of kappa scores for the *FGADR* and *EyePACS* data. We can see that the networks tend to achieve higher performance given more epochs.

Table VII presents the results for transformer-based model. We can see that, integrating high level attention mechanism with *G-Net* has improved both classification accuracy and kappa scores for all three grading datasets. In table VIII, we compared our best lesion attentive disease grading models (one each for CNN-based and Transformer-based methods) with

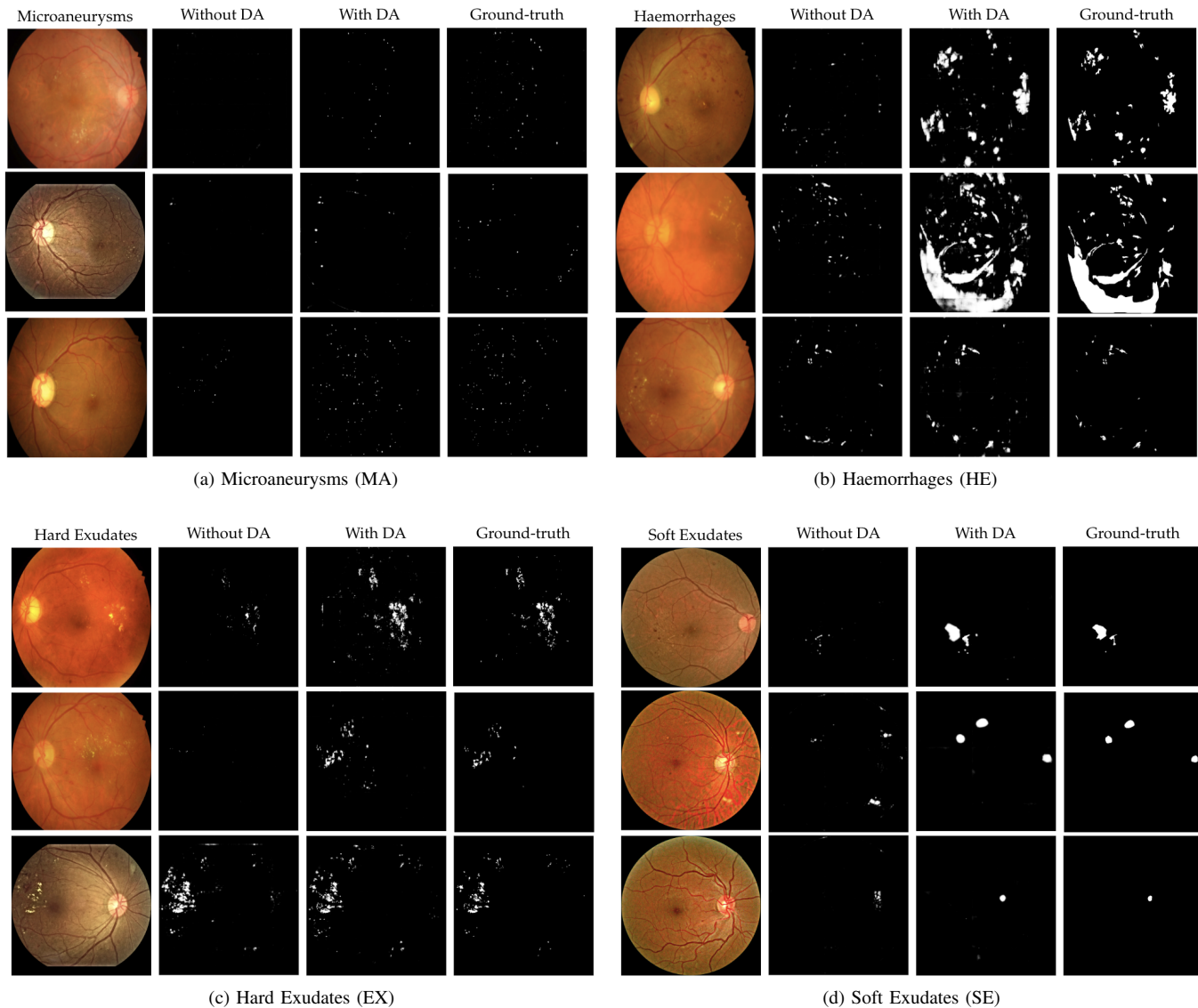


Fig. 12: Qualitative multi-lesion segmentation results for four different lesion classes. Comparison of lesion maps predicted by the segmentation models trained without (with) Domain Adaption (DA) S-Net (S-Net + AD-Net + W-Net).

TABLE VI: Performance of the proposed attention mechanisms on the CNN-based architecture (ResNet-50). Results are evaluated on three datasets *IDRID*, *EyePACS*, and *FGADR*.

Methods	IDRID		EyePACS		FGADR	
	Accuracy	Kappa	Accuracy	Kappa	Accuracy	Kappa
G-Net (ResNet-50)	0.823	0.844	0.836	0.819	0.807	0.751
G-Net + Attention (low-level)	0.897	0.904	0.881	0.867	0.860	0.852
G-Net + Attention (high-level)	0.859	0.873	0.862	0.849	0.839	0.827
G-Net + Attention (two-level)	0.904	0.911	0.895	0.883	0.872	0.861

TABLE VII: Performance of the proposed attention mechanisms on the Vision Transformer architecture (MIL-VIT). Results are evaluated on three datasets *IDRID*, *EyePACS*, and *FGADR*. Because MIL-VIT already integrated attentions at the feature-level, we only extend it with the high-level case.

Methods	IDRID		EyePACS		FGADR	
	Accuracy	Kappa	Accuracy	Kappa	Accuracy	Kappa
G-Net (MIL-VIT)	0.780	0.824	0.755	0.791	0.751	0.781
G-Net + Attention (high-level)	0.822	0.841	0.819	0.849	0.797	0.826

recent competitive methods: *JCS* (Wu et al. (2021)), Denoising Attention Fusion Network (*AFN-Net*) Zhou et al. (2020))

and Collaborative DR grading (*CoLL*) Zhou et al. (2019). Results of our CNN-based attention model G-Net (CNN) +

TABLE VIII: Comparison of our lesion attentive disease grading models with other *state-of-the-art* techniques. These methods are also used lesion information in solving the DR grading task.

Methods	IDRID		EyePACS		FGADR	
	Accuracy	Kappa	Accuracy	Kappa	Accuracy	Kappa
JCS Wu et al. (2021)	-	-	0.886	0.877	0.856	0.842
AFN-Net Zhou et al. (2020)	-	-	0.861	0.856	0.836	0.784
CoLL Zhou et al. (2019)	0.913	0.904	0.891	0.872	0.86	0.848
G-Net (MIL-ViT) + Attention	0.822	0.841	0.819	0.849	0.797	0.826
G-Net (ResNet-50) + Attention	0.904	0.911	0.895	0.883	0.872	0.861

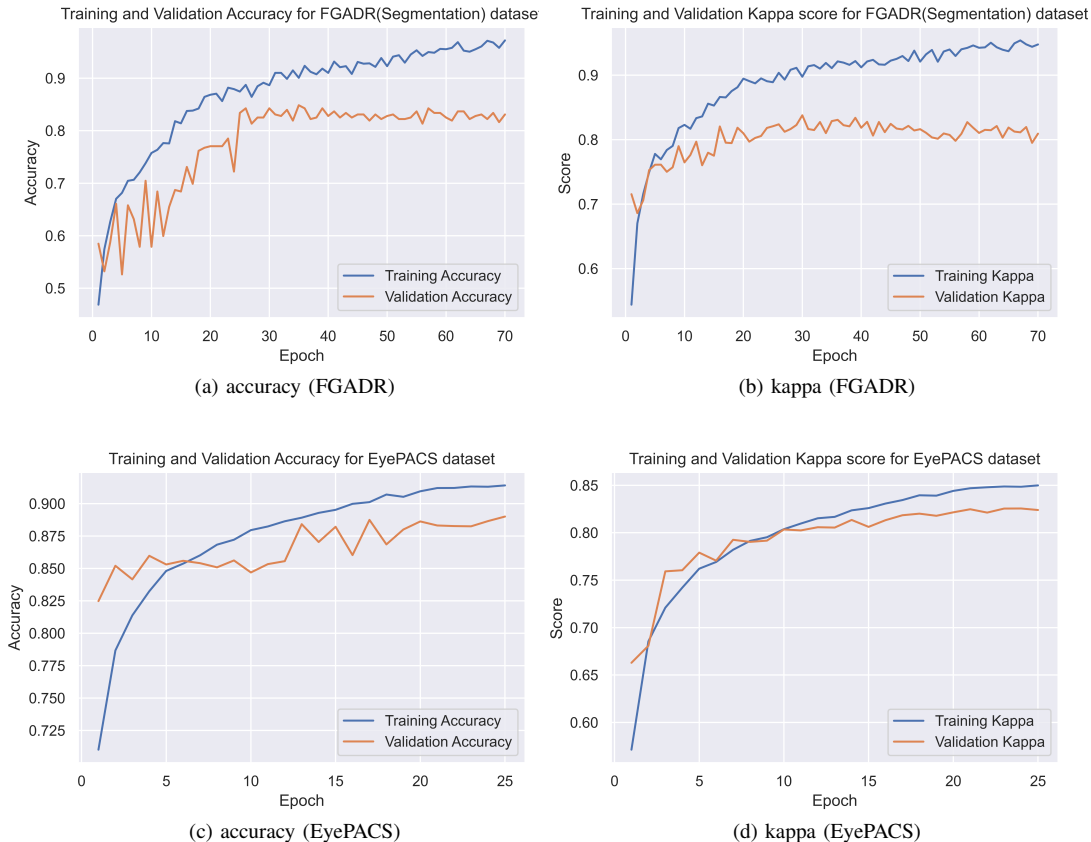


Fig. 13: Illustration our training and validation classification accuracy and kappa measurement using G-Net + Attention (two levels). Plots in the top row (a) and (b) are the accuracy and kappa score curve in *FGADR* dataset. Plots in the bottom row (c) and (d) are results in *EyePACS* dataset.

Attention on *IDRID* is comparable with the other methods. For *EyePACS* and *FGADR* dataset, we outperform other methods by around 2% in accuracy and kappa scores.

2) *DR Grading Prediction with Explainable Property*: To construct an explainable intelligent decision support system for diabetic retinopathy diagnosis, in the inference step, along with the predicted class output, we compute the class activation map (CAM) for the input image. CAM highlights the discriminative regions for the predicted class based on which the deep neural model has taken its decision. For DR grading tasks, different lesion regions observed in retinal fundus image are the key clinical factors to diagnose the patient disease progression to a particular grading class. Figure 15 illustrates an example of the explainable prediction in our system. For a given fundus image, our domain invariant lesion generator model *S-Net* predicts lesion maps for four different lesion classes (figure

15 (j) to 15 (l)). Then the attention-based grading model *G-Net* provides the disease grade and its decision explanation in the form of class activation map (figure 15 (b)). By comparing the CAM region with the predicted lesion positions, we can compare the quality of the model explanation. Intuitively, the overlapping rate of CAM on lesion maps and input images can provide explanation properties to the experts about the network’s decisions (figure 15 (c) and 15 (d)).

In figure 17, we qualitatively compare the explanation results between the grading model that is trained only using classification loss in *G-Net* settings and our proposed attention based grading model that incorporate both low-level and high-level attention concepts in settings *G-Net* (CNN) + Attention (two-level). For some typical images and their lesion maps, we discover that our attention-based grading (figure 17 (d)) was able to capture almost all the

important lesion regions whereas *G-Net* (figure 17 (c)) failed to capture these lesion regions and considered some irrelevant positions as the class discriminating mapping. In opposite, even some tiny lesion regions are also considered in the prediction decision of our grading model.

F. Performance of Trained System using User Feedback

Method	% direct user feedback	Accuracy	Kappa	Explanation
G-Net + Attention	0%	0.773	0.781	0.272
	10%	0.786	0.801	0.295
	20%	0.822	0.838	0.331
	30%	0.841	0.853	0.363
	40%	0.850	0.863	0.366
	50%	0.855	0.866	0.387

TABLE IX: Performance of our framework utilizing increasingly user-feedback. We iteratively fine-tune the model using simulated user-feedback. Experiments are conducted on *FGADR* dataset.

Within our interactive framework, given an input image, ophthalmologists can validate predicted lesion feature maps and grading class outputs, as well as provide feedback on these predictions. For example, if the predicted lesion maps have false positive or false negative regions, they can highlight the region and upon verification, these lesion maps can be used to further fine-tune our intelligent diagnosis system. As discussed in section V-B, we can use these expert annotations directly to improve the performance of our lesion attentive grading model. In order to evaluate the effect of expert’s validation and feedback process on our learning system, we conducted experiments by simulating user-feedback action. For this, we used *FGADR* dataset to simulate user feedback because this dataset has both annotations for lesion maps and grading tasks.

In figure 14, we illustrate our data split approach for user-feedback simulation. The original training data is divided into two equal splits. The disease grading model *G-Net* in beginning is trained using a half of training data and their lesion masks predicted by *S-Net*. The rest of training data is divided into five parts serving as increasingly data collected from users. After each update, a new model will be tested again on the fixed hold-out test set to justify performance. In our setting, instead of directly utilizing ground-truth samples as user feedback, we assumed that these data contain a certain noise level. This assumption makes sense in practice as we cannot guarantee accurate annotations from the user in all cases. Therefore, we simulated this scenario by applying some morphological operations on the ground-truth data and used them in the fine-tuning step. Specifically we randomly applied erosion and dilation operations for the lesion maps with a kernel size 15. Figure 16 demonstrates the effect of these operations on a ground-truth lesion mask.

Table IX presents our obtained results on *FGADR* data for the DR classifier network with rising user feedback data. At each stage, 10% of additional simulated user-feedback data is used to fine-tune a current stage of the grading network. We report both classification and explanation scores in our experiments, where the explanation score is computed based on the overlapping between the network’s heatmap regions and detected lesion positions using the Jaccard similarity (Murphy

(1996)). Table IX demonstrates to us a trend of improvement in both classification and explanation scores given enlarged user-feedback data. For example, with 30% or more response data, we achieved comparable scores against the other competitive methods discussed previously. In summary, these tests show that the system can improve even further if there are feedback from users, and these feedback can be provided with very little effort from the users.

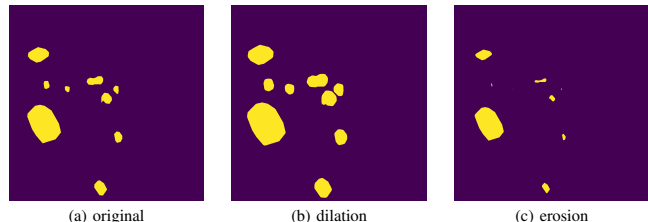


Fig. 16: Illustration of noisy user-feedback on lesion feature maps. To simulate the user behaviour, we add randomly noises by performing dilation and erosion on original lesion masks and training models using these perturbed data. The examples are (a) original segmentation map, (b) lesion map after performing dilation, and (c) lesion map after erosion morphological operations using kernel size 15.

CONCLUSIONS AND FUTURE WORKS

This work provides a unified system for DR grading, which simultaneously learns to predict the disease grading and important lesion features. The method can automatically detect different types of lesions across domains while using only annotations in the source domain and unlabeled data in the target domain. This allows for the rapid deployment of applications in new datasets without the need for extensive pixel-level annotation, which is often expensive and time-consuming to prepare. The attention network component of the proposed method identifies and exploits the most significant lesion locations for improving performance and for explainability. It also makes the annotation progress more comfortable for users and make neural networks more robust in the presence of noise in new data. Moreover, the model also offers a variety of interpretative outputs to the user, such as DR Grading prediction, lesion positions, heatmap activation of the network, and the overlapping between these regions. However, there are various aspects that can be improved and explored.

First, even though our approach has integrated lesion information for the DR Grading task, there is still another medical criterion that can be utilized to improve performance. For instance, extensive characteristics of the lesion regions such as geometry, area, radius, or the degree of occurrence of different types of lesions, are other essential factors that need to formulate during the learning strategies. However, expressing such constraints is not straightforward since most of them are not differentiable, making end-to-end learning unfeasible. Fortunately, recent advances in machine learning subjects like discrete optimization (Pogančić et al. (2019)), geometric deep learning (Monti et al. (2017); Bronstein et al.

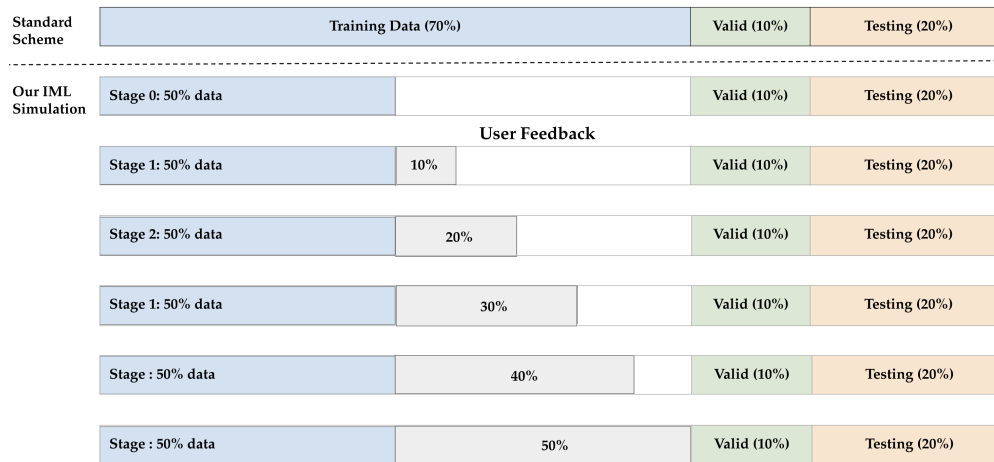


Fig. 14: Illustration of user-feedback simulation on slices of data. In a standard scheme, traditional data split strategy is followed. In our interactive simulation case, we initially split the training data into two equal parts, and used one part of the split (50% of training data) to train our proposed attention-based grading model. For the remaining part of 50% training data, it is further split into five equal slices, serving for increasingly data feedback. After each time getting data feedback, the model is fine-tuned using both initial data and new ones. The performance of a new model then is evaluated on the hold-out testing set.

(2021), and physic-informed machine learning Karniadakis et al. (2021) may offer us viable methods for incorporating these restrictions. For that reason, we believe that expanding our suggested method in those directions is worth investigating.

Second, the lack of training data is a primary obstacle that hinders the robustness and generalizability of a trained deep network. While we proposed techniques based on transfer learning and domain adaptation to alleviate these challenges, having a powerful pre-trained model is still in high demand. Currently, self-supervised learning methods trained on large-scale unlabeled data, namely the foundation model, have succeeded in various downstream tasks in natural language processing with well-known models such as BERT Dosovitskiy et al. (2021), DALL-E Ramesh et al. (2021), and GPT-3 Brown et al. (2020). This raises the question of whether foundation models trained on large-scale medical datasets can bring similar performance for downstream medical tasks Nguyen et al. (2022c). In our setting, given such a foundation model, we expect to advance accuracy for neural networks in both lesion generator and DR Grading tasks, yielding increasing the performance of the whole system and reducing user efforts in preparing data annotations.

Third, our proposed method can be applied to other medical applications such as brain tumor Nguyen et al. (2017, 2022a); Li et al. (2022) or skin cancer detection Esteva et al. (2017) where jointly localizing lesion information and data classification plays a crucial one. Therefore, designing experiments for these scenarios is an important aspect to validate the algorithm’s generalization.

Last but not least, this study organized experiments to confirm that the proposed method grows accuracy over time when provided user feedback in weakly-supervised forms. However, because these results are simulated in the computer

system, they may not cover all real scenarios in practice. This encourages us to build a real intelligent user interface and deploy it for real-world applications. Such a system when operating in practice requires overcoming various barriers. For example, developing a user-friendly and intuitive UI/UX system so that experts easily engage with and provide feedback to systems. When experts are in the annotation step, equipping computer-aided detection (CAD) Yanase and Triantaphyllou (2019) to discover and recommend similar marked locations to users is also necessary to save time and accelerate the progress. Finally, when there is a large amount of data feedback accessible, it poses concerns about learning for new instances while not forgetting past samples. Such questions are active topic research in continual learning and active learning, which is also a future direction for investigation.

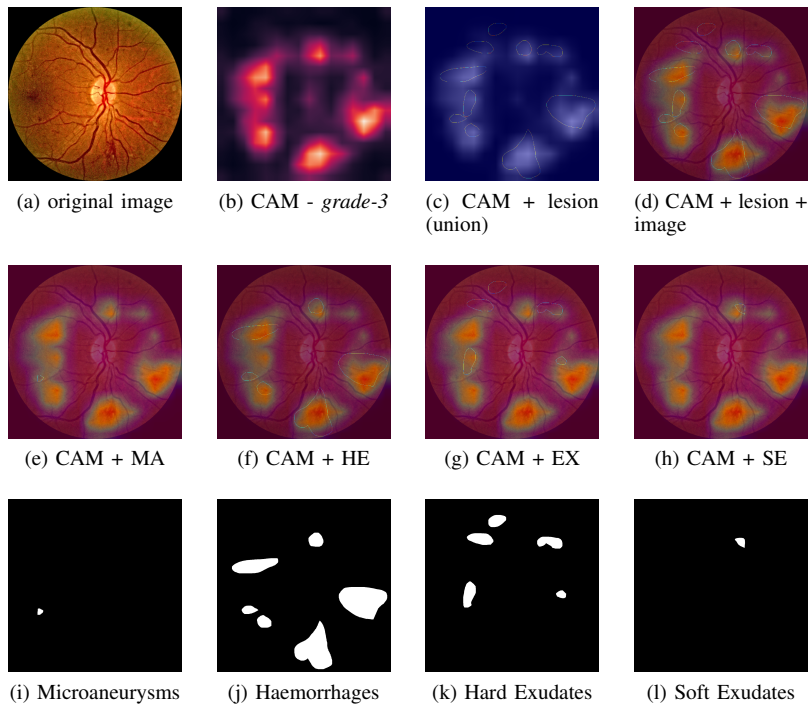


Fig. 15: For an input retina fundus image (a), we provide the lesion maps for four lesion classes (the bottom row). In the top row, the network provides a (b) class activation map (CAM) for the predicted class (*grade-3*) (c) the overlap of CAM with the union of the predicted lesion maps, and (d) overlapping of CAM and union of predicted lesion maps on the original input image. In the second row, the CAM overlap with each of the lesion maps.

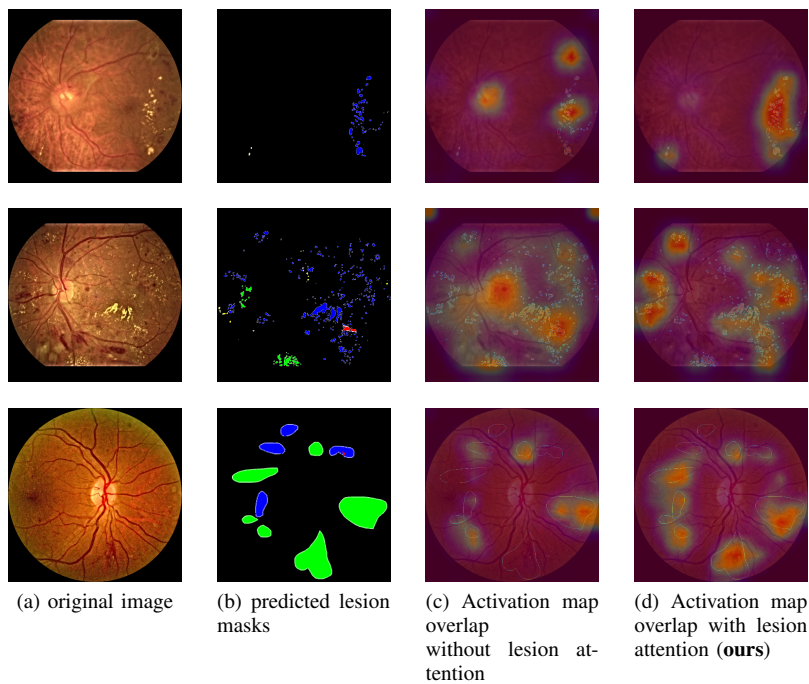


Fig. 17: Comparison on explainability of the disease classification model trained with and without lesion attention. (a) original inputs, (b) union of ground-truth lesion maps, (c) overlapping of class activation map (CAM) of the predicted grading class with the (a) and (b) for *G-Net* trained without lesion attention model *Att-Net*, (d) overlapping of class activation map (CAM) of the predicted grading class with the (a) and (b) for *G-Net* trained with lesion attention model *Att-Net*. We can observe that CAMs in column (d) overlaps with most of the lesion regions.

REFERENCES

- Abnar, S., Zuidema, W., 2020. Quantifying attention flow in transformers, in: Proceedings of the 58th Annual Meeting of the Association for Computational Linguistics, Association for Computational Linguistics, Online. pp. 4190–4197. URL: <https://aclanthology.org/2020.acl-main.385>, doi:10.18653/v1/2020.acl-main.385.
- Al-Masni, M.A., Kim, D.H., Kim, T.S., 2020. Multiple skin lesions diagnostics via integrated deep convolutional networks for segmentation and classification. *Computer methods and programs in biomedicine* 190, 105351.
- Alban, M., Gilligan, T., 2016. Automated detection of diabetic retinopathy using fluorescein angiography photographs. Report of standford education .
- Amershi, S., Cakmak, M., Knox, W.B., Kulesza, T., 2014. Power to the people: The role of humans in interactive machine learning. *Ai Magazine* 35, 105–120.
- Antal, B., Hajdu, A., 2012. An ensemble-based system for microaneurysm detection and diabetic retinopathy grading. *IEEE transactions on biomedical engineering* 59, 1720–1726.
- Arjovsky, M., Chintala, S., Bottou, L., 2017. Wasserstein generative adversarial networks, in: International conference on machine learning, PMLR. pp. 214–223.
- Bronstein, M.M., Bruna, J., Cohen, T., Velicković, P., 2021. Geometric deep learning: Grids, groups, graphs, geodesics, and gauges. *arXiv preprint arXiv:2104.13478* .
- Brown, T., Mann, B., Ryder, N., Subbiah, M., Kaplan, J.D., Dhariwal, P., Neelakantan, A., Shyam, P., Sastry, G., Askell, A., et al., 2020. Language models are few-shot learners. *Advances in neural information processing systems* 33, 1877–1901.
- Chen, L.C., Papandreou, G., Kokkinos, I., Murphy, K., Yuille, A.L., 2017. Deeplab: Semantic image segmentation with deep convolutional nets, atrous convolution, and fully connected crfs. *IEEE transactions on pattern analysis and machine intelligence* 40, 834–848.
- Chen, X., Duan, Y., Houthoofd, R., Schulman, J., Sutskever, I., Abbeel, P., 2016. Infogan: Interpretable representation learning by information maximizing generative adversarial nets. *Advances in neural information processing systems* 29.
- Cheplygina, V., 2019. Cats or cat scans: Transfer learning from natural or medical image source data sets? *Current Opinion in Biomedical Engineering* 9, 21–27.
- Dai, L., Wu, L., Li, H., Cai, C., Wu, Q., Kong, H., Liu, R., Wang, X., Hou, X., Liu, Y., et al., 2021. A deep learning system for detecting diabetic retinopathy across the disease spectrum. *Nature communications* 12, 1–11.
- Dosovitskiy, A., Beyer, L., Kolesnikov, A., Weissenborn, D., Zhai, X., Unterthiner, T., Dehghani, M., Minderer, M., Heigold, G., Gelly, S., et al., 2021. An image is worth 16x16 words: Transformers for image recognition at scale. *International Conference on Learning Representations (ICLR)* .
- Esteva, A., Kuprel, B., Novoa, R.A., Ko, J., Swetter, S.M., Blau, H.M., Thrun, S., 2017. Dermatologist-level classification of skin cancer with deep neural networks. *nature* 542, 115–118.
- EyePACS, 2015. Eyepacs challenge kaggle diabetic retinopathy dataset. <https://www.kaggle.com/c/diabetic-retinopathy-detection/data>. Accessed: 2021-10-12.
- Goodfellow, I., Pouget-Abadie, J., Mirza, M., Xu, B., Warde-Farley, D., Ozair, S., Courville, A., Bengio, Y., 2014. Generative adversarial nets. *Advances in neural information processing systems* 27.
- Gretton, A., Borgwardt, K.M., Rasch, M.J., Schölkopf, B., Smola, A., 2012. A kernel two-sample test. *The Journal of Machine Learning Research* 13, 723–773.
- Gulrajani, I., Ahmed, F., Arjovsky, M., Dumoulin, V., Courville, A.C., 2017. Improved training of wasserstein gans. *Advances in neural information processing systems* 30.
- Gulshan, V., Peng, L., Coram, M., Stumpe, M.C., Wu, D., Narayanaswamy, A., Venugopalan, S., Widner, K., Madams, T., Cuadros, J., et al., 2016. Development and validation of a deep learning algorithm for detection of diabetic retinopathy in retinal fundus photographs. *Jama* 316, 2402–2410.
- He, K., Zhang, X., Ren, S., Sun, J., 2016. Deep residual learning for image recognition, in: Proceedings of the IEEE conference on computer vision and pattern recognition, pp. 770–778.
- He, X., Yang, X., Zhang, S., Zhao, J., Zhang, Y., Xing, E., Xie, P., 2020. Sample-efficient deep learning for covid-19 diagnosis based on ct scans. *medrxiv* .
- Hung, W.C., Tsai, Y.H., Liou, Y.T., Lin, Y.Y., Yang, M.H., 2018. Adversarial learning for semi-supervised semantic segmentation. *Proceedings of the British Machine Vision Conference (BMVC)* .
- Islam, M., Vibashan, V., Jose, V., Wijethilake, N., Utkarsh, U., Ren, H., 2019. Brain tumor segmentation and survival prediction using 3d attention unet, in: International MICCAI Brainlesion Workshop, Springer. pp. 262–272.
- Isola, P., Zhu, J.Y., Zhou, T., Efros, A.A., 2017. Image-to-image translation with conditional adversarial networks, in: Proceedings of the IEEE conference on computer vision and pattern recognition, pp. 1125–1134.
- Jadon, S., 2020. A survey of loss functions for semantic segmentation, in: 2020 IEEE Conference on Computational Intelligence in Bioinformatics and Computational Biology (CIBCB), IEEE. pp. 1–7.
- Jalwana, M.A., Akhtar, N., Bennamoun, M., Mian, A., 2021. Cameras: Enhanced resolution and sanity preserving class activation mapping for image saliency, in: Proceedings of the IEEE/CVF Conference on Computer Vision and Pattern Recognition, pp. 16327–16336.
- Karniadakis, G.E., Kevrekidis, I.G., Lu, L., Perdikaris, P., Wang, S., Yang, L., 2021. Physics-informed machine learning. *Nature Reviews Physics* 3, 422–440.
- Le, N., Le, T., Yamazaki, K., Bui, T., Luu, K., Savides, M., 2021. Offset curves loss for imbalanced problem in medical segmentation, in: 2020 25th International Conference on Pattern Recognition (ICPR), IEEE. pp. 9189–9195.
- Li, J.P., Khan, S., Alshara, M.A., Alotaibi, R.M., Mawuli, C., et al., 2022. Dacbt: deep learning approach for classification

- of brain tumors using mri data in iot healthcare environment. *Scientific Reports* 12, 1–14.
- Li, K., Wu, Z., Peng, K.C., Ernst, J., Fu, Y., 2018a. Tell me where to look: Guided attention inference network, in: *Proceedings of the IEEE Conference on Computer Vision and Pattern Recognition*, pp. 9215–9223.
- Li, L., Verma, M., Nakashima, Y., Kawasaki, R., Nagahara, H., 2020. Joint learning of vessel segmentation and artery/vein classification with post-processing, in: *Medical Imaging with Deep Learning*, PMLR. pp. 440–453.
- Li, X., Chen, H., Qi, X., Dou, Q., Fu, C.W., Heng, P.A., 2018b. H-denseunet: hybrid densely connected unet for liver and tumor segmentation from ct volumes. *IEEE transactions on medical imaging* 37, 2663–2674.
- Lin, Z., Guo, R., Wang, Y., Wu, B., Chen, T., Wang, W., Chen, D.Z., Wu, J., 2018. A framework for identifying diabetic retinopathy based on anti-noise detection and attention-based fusion, in: *International Conference on Medical Image Computing and Computer-Assisted Intervention*, Springer. pp. 74–82.
- Liu, C., Belkin, M., 2018. Accelerating sgd with momentum for over-parameterized learning. *arXiv preprint arXiv:1810.13395*.
- Liu, H., Gu, X., Samaras, D., 2019. Wasserstein gan with quadratic transport cost, in: *Proceedings of the IEEE/CVF international conference on computer vision*, pp. 4832–4841.
- Long, J., Shelhamer, E., Darrell, T., 2015. Fully convolutional networks for semantic segmentation, in: *Proceedings of the IEEE conference on computer vision and pattern recognition*, pp. 3431–3440.
- Ma, A., Li, J., Lu, K., Zhu, L., Shen, H.T., 2021. Adversarial entropy optimization for unsupervised domain adaptation. *IEEE Transactions on Neural Networks and Learning Systems*.
- Maadi, M., Akbarzadeh Khorshidi, H., Aickelin, U., 2021. A review on human–ai interaction in machine learning and insights for medical applications. *International journal of environmental research and public health* 18, 2121.
- McHugh, M., 2012. interrater reliability: the kappa statistic. *biochemica medica*, 22 (3), 276–282.
- Mehta, S., Mercan, E., Bartlett, J., Weaver, D., Elmore, J.G., Shapiro, L., 2018. Y-net: joint segmentation and classification for diagnosis of breast biopsy images, in: *International Conference on Medical Image Computing and Computer-Assisted Intervention*, Springer. pp. 893–901.
- Mirza, M., Osindero, S., 2014. Conditional generative adversarial nets. *arXiv preprint arXiv:1411.1784*.
- Monti, F., Boscaini, D., Masci, J., Rodola, E., Svoboda, J., Bronstein, M.M., 2017. Geometric deep learning on graphs and manifolds using mixture model cnns, in: *Proceedings of the IEEE conference on computer vision and pattern recognition*, pp. 5115–5124.
- Murphy, A.H., 1996. The finley affair: A signal event in the history of forecast verification. *Weather and forecasting* 11, 3–20.
- Nguyen, D.H., Nguyen, D.M., Mai, T.T.N., Nguyen, T., Tran, K.T., Nguyen, A.T., Pham, B.T., Nguyen, B.T., 2022a. Asmcnn: An efficient brain extraction using active shape model and convolutional neural networks. *Information Sciences* 591, 25–48.
- Nguyen, D.M., Mai, T.T.N., Than, N.T., Prange, A., Sonntag, D., 2021a. Self-supervised domain adaptation for diabetic retinopathy grading using vessel image reconstruction, in: *German Conference on Artificial Intelligence (Künstliche Intelligenz)*, Springer. pp. 349–361.
- Nguyen, D.M., Nguyen, D.M., Vu, H., Nguyen, B.T., Nunnari, F., Sonntag, D., 2021b. An attention mechanism using multiple knowledge sources for covid-19 detection from ct images, in: *The Thirty-Fifth AAAI Conference on Artificial Intelligence (AAAI-21), Workshop: Trustworthy AI for Healthcare*.
- Nguyen, D.M., Nguyen, T.T., Vu, H., Pham, Q., Nguyen, M.D., Nguyen, B.T., Sonntag, D., 2022b. TATL: task agnostic transfer learning for skin attributes detection. *Medical Image Analysis* 78, 102359.
- Nguyen, D.M., Vu, H.T., Ung, H.Q., Nguyen, B.T., 2017. 3d-brain segmentation using deep neural network and gaussian mixture model, in: *2017 IEEE Winter Conference on Applications of Computer Vision (WACV)*, IEEE. pp. 815–824.
- Nguyen, D.M.H., Nguyen, H., Truong, M.T.N., Cao, T., Nguyen, B.T., Ho, N., Swoboda, P., Albarqouni, S., Xie, P., Sonntag, D., 2022c. Joint self-supervised image-volume representation learning with intra-inter contrastive clustering. *arXiv preprint arXiv:2212.01893*.
- Paszke, A., Gross, S., Massa, F., Lerer, A., Bradbury, J., Chanan, G., Killeen, T., Lin, Z., Gimelshein, N., Antiga, L., Desmaison, A., Kopf, A., Yang, E., DeVito, Z., Raison, M., Tejani, A., Chilamkurthy, S., Steiner, B., Fang, L., Bai, J., Chintala, S., 2019. Pytorch: An imperative style, high-performance deep learning library, in: Wallach, H., Larochelle, H., Beygelzimer, A., d'Alché-Buc, F., Fox, E., Garnett, R. (Eds.), *Advances in Neural Information Processing Systems* 32. Curran Associates, Inc., pp. 8024–8035.
- Pogančić, M.V., Paulus, A., Musil, V., Martius, G., Rolinek, M., 2019. Differentiation of blackbox combinatorial solvers, in: *International Conference on Learning Representations*.
- Porwal, P., Pachade, S., Kamble, R., Kokare, M., Deshmukh, G., Sahasrabudhe, V., Meriaudeau, F., 2018. Indian diabetic retinopathy image dataset (idrid): a database for diabetic retinopathy screening research. *Data* 3, 25.
- Prange, A., Chikobava, M., Poller, P., Barz, M., Sonntag, D., 2017. A multimodal dialogue system for medical decision support inside virtual reality, in: *Proceedings of the 18th Annual SIGdial Meeting on Discourse and Dialogue*, pp. 23–26.
- Ramesh, A., Pavlov, M., Goh, G., Gray, S., Voss, C., Radford, A., Chen, M., Sutskever, I., 2021. Zero-shot text-to-image generation, in: *International Conference on Machine Learning*, PMLR. pp. 8821–8831.
- Ronneberger, O., Fischer, P., Brox, T., 2015. U-net: Convolutional networks for biomedical image segmentation, in: *International Conference on Medical image computing and computer-assisted intervention*, Springer. pp. 234–241.
- Ruder, S., 2016. An overview of gradient descent optimization algorithms. *arXiv preprint arXiv:1609.04747*.

- Saeedi, P., Petersohn, I., Salpea, P., Malanda, B., Karuranga, S., Unwin, N., Colagiuri, S., Guariguata, L., Motala, A.A., Ogurtsova, K., et al., 2019. Global and regional diabetes prevalence estimates for 2019 and projections for 2030 and 2045: Results from the international diabetes federation diabetes atlas. *Diabetes research and clinical practice* 157, 107843.
- Saini, A., Prasad, R., 2021. Select wisely and explain: Active learning and probabilistic local post-hoc explainability. URL: <https://arxiv.org/abs/2108.06907>, doi:10.48550/ARXIV.2108.06907.
- Sankar, M., Batri, K., Parvathi, R., 2016. Earliest diabetic retinopathy classification using deep convolution neural networks. pdf. *Int. J. Adv. Eng. Technol* 10, M9.
- Selvaraju, R.R., Cogswell, M., Das, A., Vedantam, R., Parikh, D., Batra, D., 2017. Grad-cam: Visual explanations from deep networks via gradient-based localization, in: *Proceedings of the IEEE international conference on computer vision*, pp. 618–626.
- Shannon, C.E., 2001. A mathematical theory of communication. *ACM SIGMOBILE mobile computing and communications review* 5, 3–55.
- Shen, J., Qu, Y., Zhang, W., Yu, Y., 2018. Wasserstein distance guided representation learning for domain adaptation, in: *Thirty-second AAAI conference on artificial intelligence*.
- Smith, L.N., 2017. Cyclical learning rates for training neural networks, in: *2017 IEEE winter conference on applications of computer vision (WACV)*, IEEE. pp. 464–472.
- Sonntag, D., Nunnari, F., Profitlich, H.J., 2020. The skincare project, an interactive deep learning system for differential diagnosis of malignant skin lesions. technical report. arXiv preprint arXiv:2005.09448 .
- Sonntag, D., Schulz, C., Reuschling, C., Galarraga, L., 2012. Radspeech’s mobile dialogue system for radiologists, in: *Proceedings of the 2012 ACM international conference on Intelligent User Interfaces*, pp. 317–318.
- Sonntag, D., Wennerberg, P., Buitelaar, P., Zillner, S., 2010. Pillars of ontology treatment in the medical domain.
- Sun, R., Li, Y., Zhang, T., Mao, Z., Wu, F., Zhang, Y., 2021. Lesion-aware transformers for diabetic retinopathy grading, in: *Proceedings of the IEEE/CVF Conference on Computer Vision and Pattern Recognition*, pp. 10938–10947.
- Tsai, Y.H., Hung, W.C., Schultze, S., Sohn, K., Yang, M.H., Chandraker, M., 2018. Learning to adapt structured output space for semantic segmentation, in: *Proceedings of the IEEE conference on computer vision and pattern recognition*, pp. 7472–7481.
- Tzeng, E., Hoffman, J., Saenko, K., Darrell, T., 2017. Adversarial discriminative domain adaptation, in: *Proceedings of the IEEE conference on computer vision and pattern recognition*, pp. 7167–7176.
- Tzeng, E., Hoffman, J., Zhang, N., Saenko, K., Darrell, T., 2014. Deep domain confusion: Maximizing for domain invariance. arXiv preprint arXiv:1412.3474 .
- Vu, T.H., Jain, H., Bucher, M., Cord, M., Pérez, P., 2019. Advent: Adversarial entropy minimization for domain adaptation in semantic segmentation, in: *Proceedings of the IEEE/CVF Conference on Computer Vision and Pattern Recognition*, pp. 2517–2526.
- Wang, H., Wang, Z., Du, M., Yang, F., Zhang, Z., Ding, S., Mardziel, P., Hu, X., 2020. Score-cam: Score-weighted visual explanations for convolutional neural networks, in: *Proceedings of the IEEE/CVF conference on computer vision and pattern recognition workshops*, pp. 24–25.
- Wang, Z., Yin, Y., Shi, J., Fang, W., Li, H., Wang, X., 2017. Zoom-in-net: Deep mining lesions for diabetic retinopathy detection, in: *International Conference on Medical Image Computing and Computer-Assisted Intervention*, Springer. pp. 267–275.
- Wu, Y.H., Gao, S.H., Mei, J., Xu, J., Fan, D.P., Zhang, R.G., Cheng, M.M., 2021. JCS: An explainable covid-19 diagnosis system by joint classification and segmentation. *IEEE Transactions on Image Processing* 30, 3113–3126.
- Xiao, Q., Zou, J., Yang, M., Gaudio, A., Kitani, K., Smailagic, A., Costa, P., Xu, M., 2019. Improving lesion segmentation for diabetic retinopathy using adversarial learning, in: *International Conference on Image Analysis and Recognition*, Springer. pp. 333–344.
- Yan, W., Wang, Y., Gu, S., Huang, L., Yan, F., Xia, L., Tao, Q., 2019. The domain shift problem of medical image segmentation and vendor-adaptation by unet-gan, in: *International Conference on Medical Image Computing and Computer-Assisted Intervention*, Springer. pp. 623–631.
- Yanase, J., Triantaphyllou, E., 2019. A systematic survey of computer-aided diagnosis in medicine: Past and present developments. *Expert Systems with Applications* 138, 112821.
- Yang, Y., Li, T., Li, W., Wu, H., Fan, W., Zhang, W., 2017. Lesion detection and grading of diabetic retinopathy via two-stages deep convolutional neural networks, in: *International Conference on Medical Image Computing and Computer-Assisted Intervention*, Springer. pp. 533–540.
- Yang, Y., Shang, F., Wu, B., Yang, D., Wang, L., Xu, Y., Zhang, W., Zhang, T., 2021. Robust collaborative learning of patch-level and image-level annotations for diabetic retinopathy grading from fundus image. *IEEE Transactions on Cybernetics* .
- Yu, S., Ma, K., Bi, Q., Bian, C., Ning, M., He, N., Li, Y., Liu, H., Zheng, Y., 2021. Mil-vt: Multiple instance learning enhanced vision transformer for fundus image classification, in: *International Conference on Medical Image Computing and Computer-Assisted Intervention*, Springer. pp. 45–54.
- Zhou, B., Khosla, A., Lapedriza, A., Oliva, A., Torralba, A., 2016. Learning deep features for discriminative localization, in: *Proceedings of the IEEE Conference on Computer Vision and Pattern Recognition*, pp. 2921–2929.
- Zhou, Y., He, X., Huang, L., Liu, L., Zhu, F., Cui, S., Shao, L., 2019. Collaborative learning of semi-supervised segmentation and classification for medical images, in: *Proceedings of the IEEE/CVF Conference on Computer Vision and Pattern Recognition*, pp. 2079–2088.
- Zhou, Y., Wang, B., Huang, L., Cui, S., Shao, L., 2020. A benchmark for studying diabetic retinopathy: Segmentation, grading, and transferability. *IEEE Transactions on Medical Imaging* 40, 818–828.